AN FMRI BASED METHOD FOR CHARACTERIZING SUPERFICIAL LAYER CONTAMINATION IN FNIRS SIGNALS

by

Sinem Burcu Erdoğan

B.S., in Chemical Engineering, Boğaziçi University, 2005

M.S., in Biomedical Engineering, Boğaziçi University, 2007

Submitted to the Institute of Biomedical Engineering

in partial fulfillment of the requirements

for the degree of

Doctor

of

Philosophy

Boğaziçi University

2014

ACKNOWLEDGMENTS

First of all, I would like to express my deepest gratitudes to my thesis advisor Prof. Ata Akın who put forth the great time and effort to help me find my way in academia. His generous reliance on me to take part in this exciting research area was one of the milestones of my life. I am very grateful to Prof. Ahmet Ademoğlu for his great support, motivation and guidance throughout this study. Being a witness of his scientific methodology and interests gave invaluable insights during my doctoral research.

On my path to earning a PhD degree, I feel very lucky for having met precious role-model professors, researchers and colleagues from whom I have learned to analyze not only scientific data, but also daily phenomena with deeper insight and wider perspectives. I am thankful to all of them. It was a privilege for me to be a member of BME. I would like to thank all the members of neuro-signal and neuro-optical imaging laboratories. I owe much to the harmonious group and the happy atmosphere we have formed. The financial support of TÜBİTAK and BAP are also gratefully acknowledged. My visiting periods at Drexel University and Harvard Medical School contributed much to the final product of this dissertation. I would like to thank Professors Kambiz Pourrezaei, Banu Onaral, David Boas and my eternal friend Meryem Ayşe Yücel for their great help in helping me construct the road map to answering my research questions for this disseration.

Last but not least, I would like to say a big "Thank you" to my parents and my brother for their continuous reliance and support at all times. Without their encouragement and motivation, it would have been impossible for me to finish this work. I feel very grateful also for having a lot of beloved friends and family members in my life who helped me pass through hard times with much ease. This work is dedicated to my parents.

ABSTRACT

AN FMRI BASED METHOD FOR CHARACTERIZING SUPERFICIAL LAYER CONTAMINATION IN FNIRS SIGNALS

Functional near infrared spectroscopy (fNIRS) is a method for monitoring cerebral hemodynamics with a wide range of clinical applications. fNIRS signals are contaminated with systemic physiological interferences from both the brain and superficial tissues, resulting in a poor estimation of the task related neuronal activation. In this study, we introduce an extended superficial signal regression (ESSR) method for cancelling physiology-based systemic interference in fNIRS signals. We apply and validate our method on the optically weighted BOLD signals, which are obtained by projecting the fMRI image onto optical measurement space by use of the optical forward problem. The performance of ESSR method in removing physiological artifacts is compared to i) a global signal regression (GSR) method and ii) a superficial signal regression (SSR) method. The retrieved signals from each method are compared with the neural signals that represent the "ground truth" brain activation cleaned from cerebral systemic fluctuations. We report significant improvements in the recovery of task induced neural activation with the ESSR method when compared to the other two methods with higher spatial localization, lower inter-trial variability, and higher contrast-to-noise (CNR) improvement. Our findings suggest that, during a cognitive task i) superficial scalp contribution to fNIRS signals varies significantly among different regions on the forehead and ii) using an average scalp measurement together with a local measure of superficial hemodynamics better accounts for the total systemic interference. We conclude that maximizing the overlap between the optical pathlength of superficial and deeper penetration measurements is of crucial importance for accurate recovery of the evoked hemodynamic response in fNIRS recordings.

Keywords: Hemodynamic response, systemic interference, functional near infrared spectroscopy, magnetic resonance imaging, physiological artifact removal.

ÖZET

İYKAS İŞARETLERİNDEKİ YÜZEY KATMAN KİRLİLİĞİNİ TANIMLAMAK İÇİN İMRG TABANLI BİR YÖNTEM

İşlevsel yakın kızılaltı spektroskopi (iYKAS), geniş klinik uygulamaları olan bir beyin görüntüleme yöntemidir. iYKAS işaretleri, görev ilişkili sinirsel aktivasyonun tahminini zayıflatan, beyin ve yüzey dokulardan kaynaklı sistemik fizyolojik gürültüler ile kirlidir. Bu çalışmada, fizyoloji temelli sistemik gürültüleri ortadan kaldırmak amacıyla bir genişletilmiş yüzeysel işaret regresyonu (GYİR) yöntemi sunulmaktadır. Yöntem, optik ileri yönlü problemi çözerek elde edilen ağırlıklandırılmış kan oksijen seviyesi bağımlılığı (KOSB) işaretleri üzerinde uygulandı ve doğrulandı. GYİR yönteminin fizyolojik gürültüleri temizlemedeki etkinliği i) global işaret regresyonu ve ii) yüzeysel işaret regresyonu yöntemleri ile karşılaştırıldı. Her yöntemin uygulanması sonucu sistemik fizyolojik gürültüden arındırılaran işaretler, beyinsel sistemik salınımlardan arındırılmış "doğru" beyin aktivasyonunu yansıtan sinirsel işaretler ile karşılaştırıldı. Çalışmada, GYiR yöntemi ile görev ilişkili sinirsel aktivasyonun geri kazanılmasında diğer iki yönteme göre önemli iyileşmeler bildirilmektedir. Bulgular, bilişsel bir görev esnasında i) yüzeysel deri katmanından gelen işaretin İYKAS ölçümlerine katkısının alnın farklı bölgelerinde önemli farklılıklar gösterdiği, ii) bölgesel deri kanlanması ölçümlerinin yanında ortalama bir deri kanlanması ölçümünün kullanılmasının, toplam sistemik etkiyi açıklamada daha etkili olacağı yönündedir. Yüzeysel ve daha derin iYKAS ölçümlerinin optik yolaklarının örtüşümünü maksimize etmenin, görev ilişkili hemodinamik cevabı elde etmede büyük öneme sahip olduğu sonucuna varılmıştır.

Anahtar Sözcükler: Hemodinamik cevap, sistemik etkileşim, işlevsel yakın kızılaltı spektroskopi, manyetik rezonans görüntüleme, fizyolojik gürültü temizliği.

TABLE OF CONTENTS

LIST OF FIGURES

LIST OF SYMBOLS

$\mathbf{A}$	Wavelength-specific forward operator
B	Magnetic field
C_n	Concentration of absorbent molecule
H	Magnetic field strength
$L_{i,j}$	Mean Pathlength travelled between source i and detector j
l_{DPF}	Differential pathlength factor
R^2	Pearson correlation coefficient
R_2^*	Rate of free induction decay
S_0	Proton density
T_2^*	Free induction decay
T_E	Echo time
T_R	Repetition time
V	Resting venous volume fraction
y	Measurement time series
Y	Fractional oxygenation
Y_{Brain}	Brain Signal
Y_{Global}	Global Signal
Y_{Neural}	Neural Signal
Y_{Sum}	Sum Signal
$Y_{Superficial}$	Superficial Signal
χ	Magnetic susceptibility
ε	Wavelength-dependent extinction coefficient
γ	gyromagnetic ratio
λ	Wavelength
μ	Mean
μ_0	Magnetic permeability
μ_a	Absorption coefficient
μ_s	Scattering coefficient

ϕ	Average intensity of light
σ	Standard deviation
θ	Flip angle

LIST OF ABBREVIATIONS

BOLD	Blood Oxygenation Level Dependent
CBV	Cerebral Blood Volume
$CMRO_2$	Cerebral Metabolic Rate of Oxygen
CNR	Contrast-to-noise ratio
CSF	Cerebral Spinal Fluid
CV	Coefficient of Variation
ESSR	Extended Superficial Signal Regression
GM	Gray Matter
fMRI	Functional Magnetic Resonance Imaging
fNIRS	Functional Near Infrared Spectroscopy
GSR	Global Signal Regression
HbO	Oxyhemoglobin
HbR	Deoxyemoglobin
HbT	Total Hemoglobin
Hct	Hematocrit
LFOs	Low Frequency Oscillations
LED	Light Emitting Diode
MBLL	Modified Beer-Lambert Law
MPRAGE	Magnetization Prepared Rapid Gradient Echo
MRI	Magnetic Resonance Imaging
MSE	Mean Squared Error
MTT	Mean Transit Time
NIRS	Near Infrared Spectroscopy
OD	Optical Density
PET	Positron Emission Tomography
PPL	Mean Partial Pathlength
SD	Source-detector
SPM	Statistical Parametric Mapping

SSR	Superficial Signal Regression
VLFOs	Very Low Frequency Oscillations
WM	White Matter

1. INTRODUCTION

1.1 Motivation and Objectives

Functional near infrared spectroscopy (fNIRS) is a non-invasive imaging modality that utilizes near-infrared light for monitoring hemodynamic changes associated with evoked brain activity [1, 2, 3]. Over the past 15 years, fNIRS has become a complementary and alternative technique to functional Magnetic Resonance Imaging (fMRI) with a high potential of use for clinical studies, cognitive, behavioral and neuroscience research [4, 5, 6]. The advantages of fNIRS for studying brain activation include cost efficiency, possibility of use at the bedside, good temporal resolution, measurement of both oxy- and deoxyhemoglobin and use of non-ionizing radiation while the limitations include modest spatial resolution, lack of absolute quantification in continuous wave systems and limited penetration depth [7, 8].

A major concern with fNIRS measurements is the presence of strong spontaneous fluctuations or physiology-based systemic interferences in the signal due to cardiac pulsation (around 1 Hz), respiration (around 0.2 to 0.3 Hz) and a variety of spontaneous low frequency oscillations (LFOs) occurring in the range of 0.01-0.1 Hz [9, 10, 11]. LFOs include the spontaneous oscillations in local vascular tone known as vasomotion [12, 13] and the systemic oscillations in arterial blood pressure known as Mayer waves which typically occur at 0.1 Hz [14]. Such systemic interferences are present in both the cerebral and superficial layers (i.e scalp and skull) of the head and reduce the accuracy of fNIRS for detecting brain activation. The contribution of systemic interference to fNIRS signal is intensified because light is both emitted and received at the surface of the scalp and this back reflection geometry increases the sensitivity of fNIRS measurements to systemic oscillations occurring in the superficial scalp tissue. Besides, while blood flow within the brain is stabilized by partial autonomic neural control [15], blood flow at the scalp tissue is not regulated by this buffer mechanism and is influenced by systemic physiological changes to a greater extent. The accurate identification and

reliable elimination of the physiological noise embedded in the fNIRS signals can improve the signal-to-noise ratio, and/or can enable the same signal-to-noise ratio with a shorter stimulus period. This goal is significant, as with decreased acquisition time and increased signal quality, larger subject populations including young children and hospitalized patients can be monitored in a shorter time while the effects of fatigue and adaptation are minimized.

Several methods have been proposed in the literature to reduce the systemic interference in fNIRS signals. Low pass filtering is the most common application, as it can effectively remove high frequency systemic oscillations such as heart beat [16, 17]. However, the frequency spectrum of physiology-based systemic interferences such as respiration, LFOs, and very low frequency oscillations (VLFOs) significantly overlap with the frequency spectrum of functional hemodynamic response to brain activation. Frequency-based removal of these interferences can therefore, distort the temporal characteristics of the recovered brain activity signal. Other methods for removing systemic interference include adaptive subtraction of a cardiac waveform [18], direct subtraction of a "nonactivated" fNIRS waveform [16], state space estimation [19, 20, 21], wavelet filtering [22, 23, 24, 25] and principal components analysis [26, 27]. There are also studies investigating the partial optical path lengths via Monte Carlo simulations of a layered human head model for multi-distance measurement set-ups [28, 29, 30].

An extension to multi-distance measurement methods includes the use of additional short source-detector (SD) distance (usually less than 1 cm) channels together with typical long SD distance (about 3 cm) channels which are sensitive to both cerebral and extracerebral tissues. Short SD distance channel measurements probe superficial, extracerebral tissue only and are dominated by physiology-based systemic interference. To isolate and extract brain specific hemodynamic changes, these short SD distance channel measurements have been used to remove systemic interference from the long SD distance channel measurements with the assumption that a common systemic interference is present in both channel measurements [33-36]. Using multiple SD separations, an adaptive cancellation method has also been recently proposed and validated [37-39].

In contrast to the necessity of using short SD distance measurements, superficial hemodynamics can also be estimated by exploiting the photon time-of-flight distribution in time-domain NIRS at the expense of high-cost equipment [40-41].

1.2 Thesis Contribution

Most of the above mentioned methods are based on the assumption that systemic interference in fNIRS measurements is spatially homogeneous across the surface of the scalp. In this dissertation; we hypothesize that the spontaneous oscillations occuring in the brain tissue have a spatially global effect, while the systemic interference coming from superficial scalp tissue has a more pronounced and localization-dependent effect on the fNIRS measurements. We treat both effects separately and propose an extended superficial signal regression method for cancelling physiology-based systemic interference that is known to obscure the functional response to brain activation. To test our hypothesis; we apply our method on an optically weighted spatial average of the fMRI blood oxygen level-dependent (BOLD) signal which is obtained by combining weighted contributions from each voxel that coincide with the photon migration path. More specifically; for each subject and SD pair; once subject specific head models are obtained from structural MRI, photon-migration theory and Monte Carlo simulations are used to estimate the spatial sensitivity profile of light absorption changes that occur within different anatomical compartments of the head. The overlap of this optical sensitivity profile with the voxels in each tissue layer (i.e. scalp, skull, CSF, gray matter and white matter) provides a means of predicting a spatially weighted BOLD response as a hemodynamic correlate of the fNIRS signal.

We evaluate the efficacy of removing systemic interference that occurs both in the brain and at the scalp tissue with our extended superficial signal regression (ESSR) method and compare its performance of physiological noise removal to i) a superficial signal regression (SSR) method where only superficial scalp interference is removed and ii) a global signal regression (GSR) method where it is assumed that systemic interference across all measurements is spatially global as proposed by most studies

[29, 31, 32, 33].

Although the data acquisition methods and signals in fNIRS and fMRI are different, it is well known that both methods are sensitive to the same hemodynamic changes. A number of studies involving concurrent fNIRS and fMRI recordings have shown that during functional brain activation, there is a strong correspondence between the local hemodynamic responses recorded by the two modalities [34, 35, 36, 37, 38]. Unlike fNIRS, fMRI has the advantage of probing brain tissue independent of the overlying scalp and skull layers. Signals from brain voxels are not mixed with superficial contamination but still are subject to cerebral systemic fluctuations interfering the brain functional response.

Exploiting the ability of fMRI to localize haemodynamic changes in the scalp for a quantification of the systemic interference is a novel approach, since information about skin haemodynamic changes is neglected in most fMRI and fMRI/fNIRS studies. To date, there have been no studies that have attempted to i) use scalp superficial interference measured by fMRI to construct a spatially weighted BOLD signal in which the true brain activity is embedded and ii) test the performance of various interference cancellation methods on an fMRI correlate of the fNIRS signal.

2. BACKGROUND

Evoked hemodynamic signals result from neural-vascular and neural-metabolic coupling to underlying changes in the electrophysiology of the brain. In this chapter, we will review the physical and physiological background for two of the hemodynamic-based neuroimaging techniques used in this work, namely functional near infrared spectroscopy (fNIRS) and functional magnetic resonance imaging (fMRI), which have been developed for measuring these underlying metabolic and vascular changes noninvasively.

2.1 Functional Near Infrared Spectroscopy (fNIRS)

The near infrared spectroscopy (NIRS) technique uses safe, low levels of light ($\sim$10 mW) within the wavelength region of 650-950 nm to make spectroscopic optical measurements of absorption changes. In this wavelength region, the absorption of light by water is relatively low (Figure 2.1) while oxy- and deoxy-hemoglobin (hereafter denoted as HbO and HbR respectively) are the dominant absorbent chromophores whose concentrations vary during functional activity. At these wavelengths, light can diffusely propagate through up to several centimeters of tissue and deep enough to penetrate to approximately the outer 5-10 mm of cerebral cortex with non-invasive measurements on the scalp surface [39, 40]. Furthermore, the difference in the near-infrared absorption spectra of HbO and HbR allows the separate measurement of the concentrations of these two species (Figure 2.1). To achieve this goal, it is sufficient to perform NIRS measurements at two wavelengths. The intensity of measured light, which has diffused through the head, is sensitive to changes in the concentration (moles per volume tissue|sample) of HbO and HbR which allows the NIRS technique to be used to monitor changes in these chromophores during functional activity.

While the sum of NIRS measures of HbO and HbR concentration changes pro-

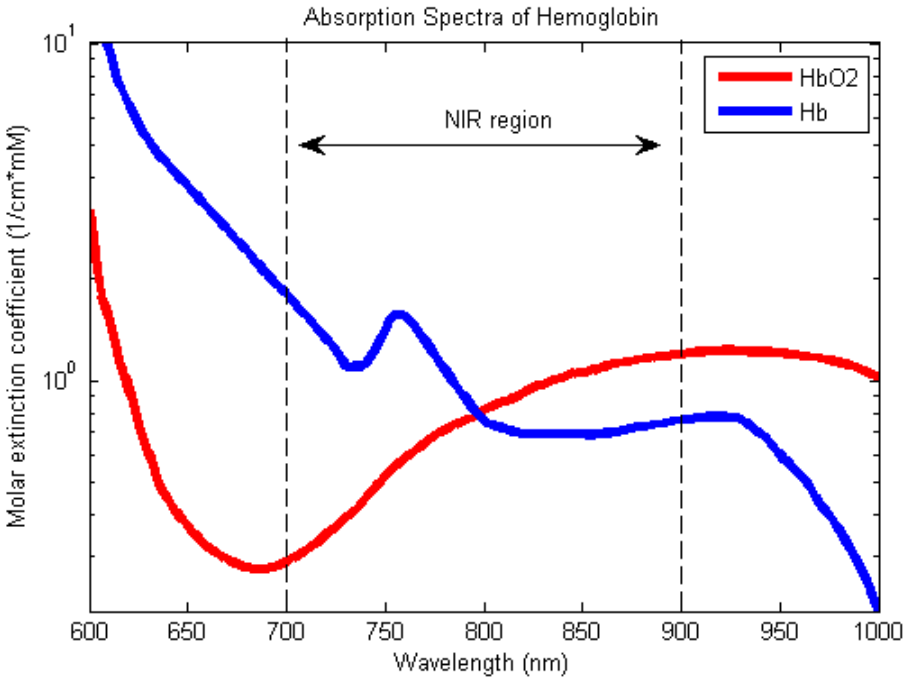

Figure 2.1 Oxy- and deoxy-hemoglobin are the two dominant biological chromophores in the near infrared region of light spectrum. The characteristic absorption spectra of these chromophores is used to infer changes in the concentration of these two species based on the spectroscopic measurement (multiple wavelengths) of absorption changes during periods of functional activity in the brain [41].

vides a measure of the cerebral blood volume (CBV) change, individual concentrations of the two forms of hemoglobin result from the interplay between physiological parameters such as regional blood volume, blood flow, and metabolic rate of oxygen consumption. Hence, NIRS offers an advantage over BOLD-fMRI which cannot disentangle blood flow and oxygen consumption changes without also acquiring blood flow images [42, 43]. This ability is important for a wide range of brain studies particularly of the developing and diseased brain.

Since the mid-1990s, NIRS technique has had a wide variety of applications for human functional brain studies. An increasing number of researchers have employed the technique to study cerebrovascular response to visual [44, 45], auditory [46], and somatosensory [16, 47] stimuli. Other areas of investigation have included the motor system [48, 49] and language [50]. Some researchers have addressed the prevention and treatment of seizures [51, 52] and psychiatric concerns such as depression [53], Alzheimer's disease [54], and schizophrenia [55, 56], as well as stroke rehabilitation

[57, 58].

While NIRS holds great promise as a tool for clinical studies, cognitive, behavioral and neuroscience research, there are limitations to its applications. The diffuse nature of photon migration through the tissue limits the penetration depth and therefore sensitivity to brain activation which occurs in the subcortical regions. The sensitivity to brain activation is further degraded by contamination from several systemic physiological signals, which can have a larger percent signal variation than that of the brain activation and in some cases may even phase-lock with the stimulation [9, 11, 12].

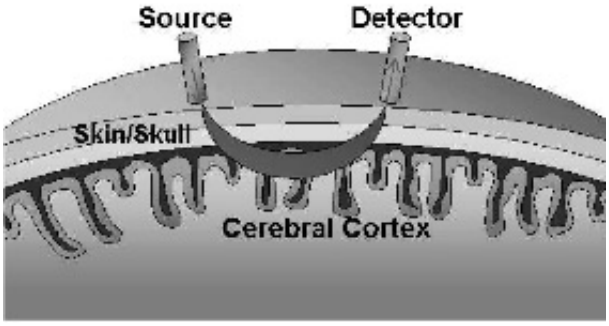

Figure 2.2 Light propagation through the head. Light is injected at the surface of the scalp, travels through extracerebral scattering tissues (i.e. scalp, skull and CSF) into the brain and again is received at the surface of the scalp. This back-reflection geometry makes NIRS measurements highly sensitive to background hemodynamic fluctuations in the superficial extracerebral tissues [59].

2.1.1 Reconstruction of Hemodynamics from NIRS Data

A typical NIRS measurement set-up for monitoring brain function consists of a grid of light sources and photon detectors which are positioned on the head of a subject. Each source-detector pair is called a "channel" or an "optode pair". Each channel measurement is obtained by non-invasively monitoring optical absorption changes of light that traverses the head going from a source to a detector. The sensitivity profile for each of these measurements is determined by modeling the propagation of light through the biological tissue and spans a volume between the source and detector

positions. An example of such a profile is shown in Figure 2.3.

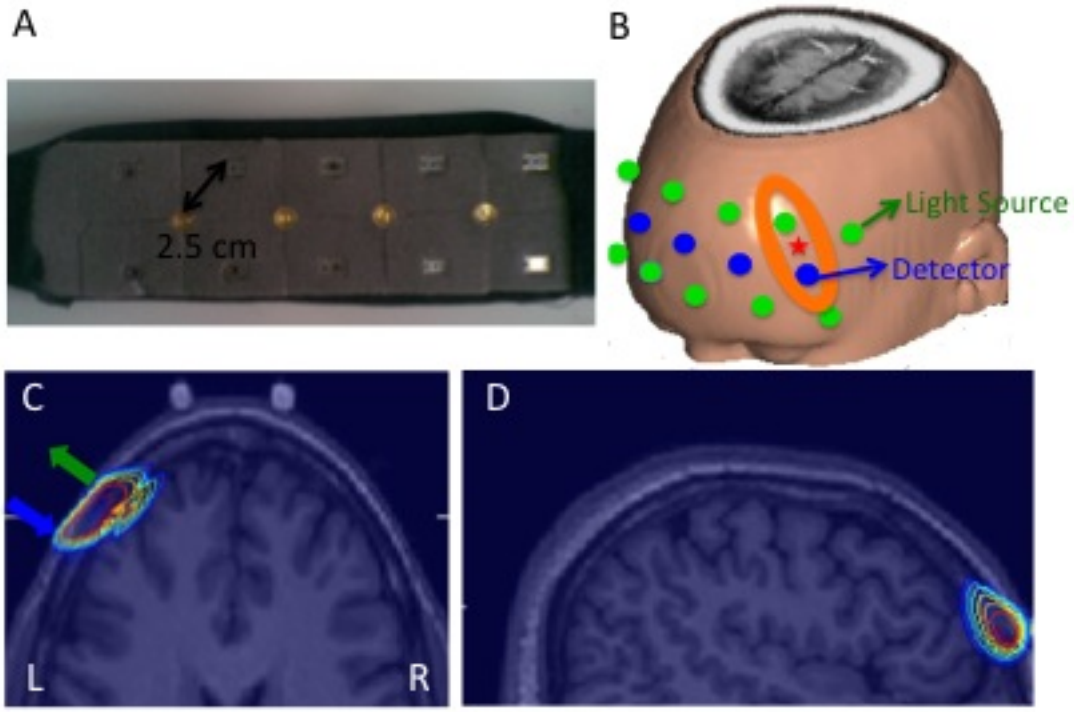

Figure 2.3 The NIRS probe used in our experiments (A). The probe is placed over the forehead (B) and monitors hemodynamic changes that occur in the first few millimeters of the prefrontal cortex. The red star in panel B shows the location of this axial slice relative to the optical probe. In panels C and D, the photon absorption sensitivity of a NIRS measurement is illustrated. The optical sensitivity profile is determined by the propagation of light transmitted from a source position and recorded by a detector placed 2.5 cm away (axial and sagittal views are presented). The contour overlay is shown in logarithmic scale and contours are presented for each order of magnitude.

During the performance of a task, increased brain activity leads to functional changes in the concentrations of HbO and HbR which eventually result in changes in the absorption of near infrared light within the tissue. These absorption changes are spatially integrated over the diffuse path of the light, giving rise to the measured changes in the intensity of light at the surface of the head. The change in light absorption or optical density (ΔOD) can then be calculated from the normalized changes in the light incident on a detector. ΔOD is defined as

$$\Delta OD_{i,j}(t,\lambda) = -Ln\left[\frac{\Phi_{i,j}(t,\lambda)}{\Phi_{i,j}(0,\lambda)}\right] = \int_{r(\gamma)} \Delta\mu_{abs}(r)\cdot dr \tag{2.1}$$

$$\Phi_{i,j}(t,\lambda) = \int_{r(\gamma)} \Phi_{i,j}(0,\lambda)\cdot e^{-\mu_{abs(r)}}\cdot dr \tag{2.2}$$

where $\Phi_{i,j}$(t,λ) describes the light emitted from a source position i, which becomes incident on a given detector j. The integrals in Eq. 2.1 and Eq. 2.2 are functional path integrals over the ensemble of possible photon trajectories through the tissue [7].

For a typical functional hemodynamic measurement, absorption changes within the probed tissue are assumed to be small and do not perturb the path of light through the tissue. This approximation is reasonable for typical hemoglobin changes observed during moderate functional activity, which are only a several percent change in hemoglobin concentration and represent small perturbations of the background absorption [60]. With this approximation, absorption changes can be expressed as a linear combination of the changes in HbO and HbR concentrations, by replacing the path integral in Eq. 2.1 with the multiplication by a mean pathlength term ($L_{i,j}$). The changes in optical density measured as each wavelength of light are given by the Beer-Lambert law [61, 62, 63]:

$$\Delta OD_{i,j}(t,\lambda) \approx L_{i,j}(\lambda) \cdot \sum_{r=1}^{Nvox} \Delta\mu_r(t,\lambda) \tag{2.3}$$

$$\Delta OD_{i,j}(\lambda) = L_{i,j}(\lambda) \cdot (\varepsilon_{HbR}(\lambda) \cdot \Delta[HbR] + \varepsilon_{HbO}(\lambda) \cdot \Delta[HbO]) \tag{2.4}$$

The variable ε is the wavelength-dependent extinction coefficient for each hemoglobin species and $L_{i,j}$ is the pathlength traveled by light between the source and detector pair [i,j]. However, the Beer-Lambert law is strictly valid only in the absence of scattering[62, 64]. This is not the case for optically dense tissue like the head. The mean pathlength of light depends on the scattering properties of the underlying tissue. Thus, the modified Beer-Lambert law (MBLL) is often used to approximate the effects of scattering by accounting for the diffuse propagation of light by multiplying the linear source-detector separation by an additional differential pathlength factor (l_{DPF}) [7, 62, 64, 63]. The MBLL can be formulated as

$$\Delta OD(\lambda,t) = \sum_n \varepsilon_n(\lambda) \cdot \Delta C_n(t) \cdot L_{i,j} \cdot l_{DPF}(\lambda) \tag{2.5}$$

where $\Delta C_n(t)$ denotes the concentration change of each absorbent chromophore (hemoglobin

species) within the path of incident light. For absorption measurements at two wavelengths, hemoglobin changes are given by

$$\Delta\left[HbR\right]=\frac{\varepsilon_{HbO}\left(\lambda_2\right)\cdot\Delta OD\left(\lambda_1\right)/\left(L\cdot l_{DPF}\left(\lambda_1\right)\right)-\varepsilon_{HbO}\left(\lambda_1\right)\cdot\Delta OD\left(\lambda_2\right)/\left(L\cdot l_{DPF}\left(\lambda_2\right)\right)}{\varepsilon_{HbR}\left(\lambda_1\right)\cdot\varepsilon_{HbO}\left(\lambda_2\right)-\varepsilon_{HbO}\left(\lambda_1\right)\cdot\varepsilon_{HbR}\left(\lambda_2\right)} \tag{2.6}$$

and

$$\Delta\left[HbO\right]=\frac{\varepsilon_{HbR}\left(\lambda_1\right)\cdot\Delta OD\left(\lambda_2\right)/\left(L\cdot l_{DPF}\left(\lambda_2\right)\right)-\varepsilon_{HbR}\left(\lambda_2\right)\cdot\Delta OD\left(\lambda_1\right)/\left(L\cdot l_{DPF}\left(\lambda_1\right)\right)}{\varepsilon_{HbR}\left(\lambda_1\right)\cdot\varepsilon_{HbO}\left(\lambda_2\right)-\varepsilon_{HbO}\left(\lambda_1\right)\cdot\varepsilon_{HbR}\left(\lambda_2\right)} \tag{2.7}$$

These hemoglobin concentrations are expressed as the concentration of hemoglobin per volume of tissue. In addition, the change in total hemoglobin concentration ($\Delta\left[HbT\right]$) are calculated by the sum of oxy- and deoxy-hemoglobin changes ($\Delta\left[HbT\right]=\Delta\left[HbO\right]+\Delta\left[HbR\right]$).

In NIRS methodology, the measurement forward equation is described as the sum over all volume locations of the absorption changes weighted by the measurement sensitivity. This measurement sensitivity is illustrated in Figure 2.3, showing the sensitivity profile for one such source-detector measurement pair. Large changes in either absorption or scattering can perturb the propagation of light through the tissue changes. This creates a non-linear forward equation (reviewed in [2, 65]). However, since functional hemodynamic changes are generally small relative to background scattering and absorption, the forward equation is often linearly approximated as discussed, i.e.

$$y\left(\lambda\right)=\mathbf{A}\left(\lambda\right)\cdot\delta\left(\lambda\right) \tag{2.8}$$

In Eq. 2.8, $\mathbf{A}$ is the wavelength-specific forward operator. This matrix is formed by the measurement sensitivity profiles for each source-detector pair. is a vector of the absorption change at each volume location. In matrix form, this equation is arranged such that each measurement time series (y) is the sensitivity-weighted sum over the volume of the absorption changes.

2.1.2 Systemic Interference in fNIRS Signals

In brain fNIRS, the incident and backscattered beams cross skin, subcutaneous fat and scalp muscles, which are heavily vascularised. As a consequence, measurements are sensitive to haemodynamic changes occurring in these extracerebral tissues. The measured signals (HbR and HbO concentration changes) are a mixture of hemodynamic signals occurring in the gray matter and interfering signals occurring in these overlaying tissue layers [38, 66, 67]. Among the major sources of interference are cardiac and respiratory oscillations, which are themselves partly coupled. There are also low frequency spontaneous physiological oscillations (referred to as LFOs, vasomotor waves or Mayer's waves) around 0.1 Hz, as well as very low frequency oscillations around 0.04 Hz [9]. All of these interference sources are located both in the vasculature of the layers overlaying the brain and in the brain itself, and are often referred to as "global interference".

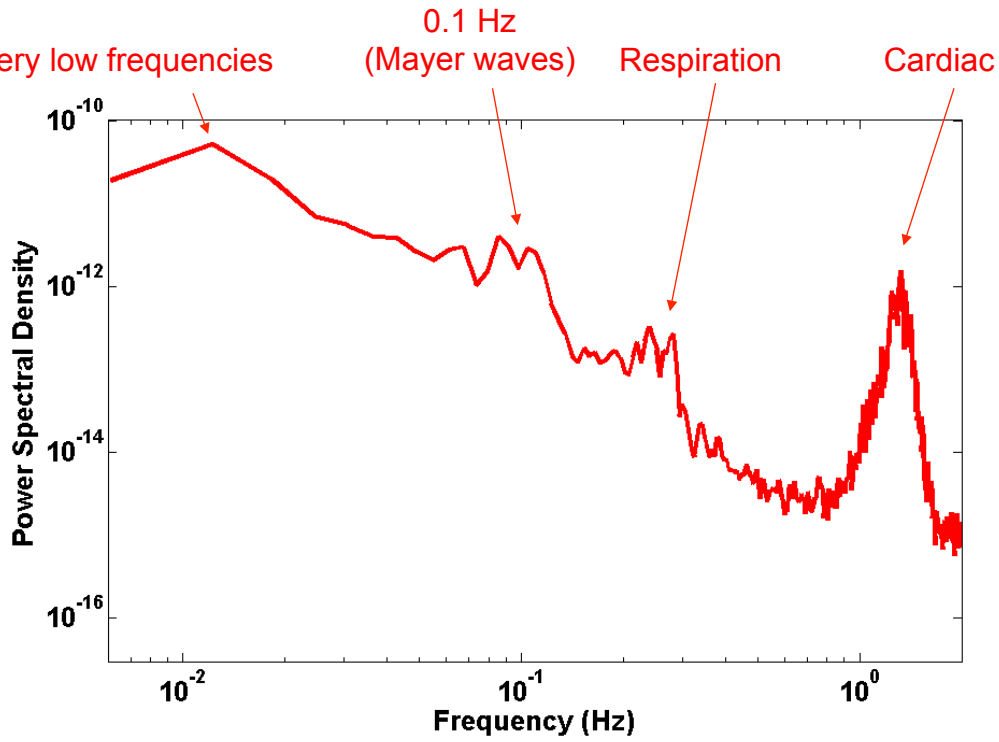

Figure 2.4 Power spectral density of physiological fluctuations in a sample fNIRS measurement.

Superficial fluctuations not only impair the signal-to-noise (SNR) ratio of fNIRS

signals, but also may be incorrectly attributed to cerebral changes, leading to false positives in fNIRS experiments. The sensitivity of fNIRS to hemodynamic changes in superficial scalp layer was estimated to be 10 to 20 times higher than to changes in deeper cortical tissue, depending on the source-detector distance and the model used for the estimation [68]. In addition, when compared to the cerebral compartment, where the blood flow is stabilized by cerebral autoregulation, the blood flow in the skin is more strongly affected by changes in the systemic physiology. Physiological noise induced by heart beat, breathing cycle, low frequency oscillations of blood pressure and heart rate around 0.1 Hz (Mayer waves) often account for more than 10% of fNIRS signal changes, leading to a lower sensitivity of fNIRS to cerebral activation as compared to fMRI [7, 69]. Moreover, task-induced changes in skin perfusion can obscure cerebral activation patterns in fNIRS experiments. Such task-evoked changes result either from systemic blood pressure changes [7] or from skin-specific regulation mechanisms. Recently it was demonstrated that blood pressure fluctuations can exert confounding effects on brain fNIRS, through expression in extracranial tissues and within the brain itself [70]. Changes in the skin blood volume might be evoked by many experimental task paradigms currently used in fNIRS studies, in particular in complex settings involving emotional and cognitive processing. Since these changes are stimulus-locked and hence cannot be separated from cortical signals by appropriate filtering, they might produce false positives in fNIRS activation maps [71, 72].

Several methods have been proposed to separate cerebral and extracranial signals in fNIRS. In a part of these methods additional measurements of superficial haemodynamics are performed which are then used to eliminate the extracranial contribution in the fNIRS signals. Extracranial hemodynamic can be estimated either by means of an additional short-distance detector [31, 73], NIRS tomography [74] or analysis of the photon time-of-flight distribution in time-domain NIRS [75]. Most of these methods rely on the assumption of a homogeneous spatial distribution of extracranial signals across the scalp. This assumption may be justified for haemodynamic fluctuations in capillaries or small vessels, but may be less accurate for the contribution of big arteries and veins supplying the scalp [76].

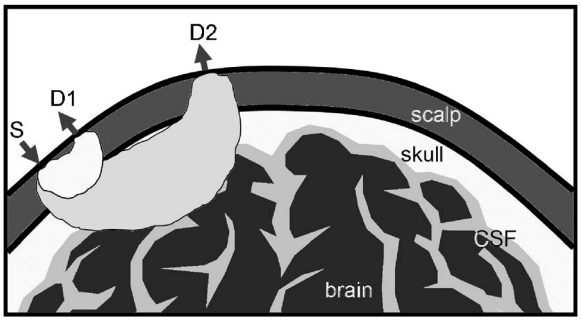

Figure 2.5 Multi-distance measurement approach. Superficial layer hemodynamics acquired from a short distance measurement between source S and detector D1 is used to estimate the systemic interference present in the long distance measurement between source S and detector D2 [32].

Another group of methods explores differences in the temporal evolution of the extra- and intracerebral haemodynamic signals. Adaptive filtering [77], statistical parametric mapping (SPM) where systemic changes were included as regressors into the model [78], independent component analysis [79] and superficial signal regression assume statistical independence of superficial and cerebral signals. However, statistical independence might be violated if skin perfusion changes are induced by the task.

2.2 Functional Magnetic Resonance Imaging (fMRI)

Functional magnetic resonance imaging (fMRI) [80, 81, 82, 83] is currently the most popular imaging technique employed for studying brain function non-invasively. The development of fMRI was fueled by the observation of the blood oxygenation level-dependent (BOLD) effect [82]. Underlying this effect are changes in HbR content resulting from changes in cerebral blood volume (CBV), cerebral blood flow (CBF), and oxygen metabolism following sensory stimulation or cognitive tasks [84, 85]. Such physiological changes are detectable with magnetic resonance imaging (MRI) because the magnetic resonance (MR) signal is sensitive to microscopic magnetic field gradients.

MRI relies on the nuclear magnetic resonance of hydrogen atoms (protons) in water. When protons are placed in a strong magnetic field and exposed to a pulse of radio waves of a particular frequency, they resonate or emit energy of the same

frequency. The resonance signal can be spatially localized by applying magnetic-field gradients in three dimensions and the localized signals can be converted to an anatomical image. The MRI signal contains information about whether the hydrogen atoms are present as free water or are partially bound in molecular structures such as white matter, gray matter. Hence, the method can differentiate various tissue types. fMRI, in contrast, monitors changes in local brain activity by measuring signals that depend on the differential magnetic properties of HbR and HbO.

Substances can be classified according to their magnetic susceptibility which can be defined as the ability of a substance to produce an internal magnetic field in response to an applied magnetic field. Magnetic field strength depends on the material property of magnetic susceptibility with the following formula:

$$B = \mu_0(H + \chi H) \tag{2.9}$$

where μ_0 is magnetic permeability, χ is magnetic susceptibility, H is the magnetic field strength and B is the magnetic field. χ can be positive or negative: paramagnetic ($\chi > 0$) and diamagnetic ($\chi < 0$).

One of the remarkable developments in recent work on magnetic resonance (MR) imaging is the recognition that changes in the metabolic state of the brain affect the local MR signal and provide an intrinsic mechanism for detecting brain activation [81, 82]. The origin of this effect is that hemoglobin is diamagnetic when oxygenated and paramagnetic when deoxygenated. The presence of HbR alters the local magnetic susceptibility, creating magnetic field distortions within and around the blood vessels, and this microscopically inhomogeneous field produces a slight alteration in the local MR signal [86]. The magnetic susceptibility of blood is affected by the level of oxygenation according to the following formula:

$$\chi_{blood} = Hct\,(Y\chi_{HbO} + (1 - Y)\,\chi_{HbR}) + (1 - Hct)\,\chi_{plasma} \tag{2.10}$$

where Hct is the hematocrit (fraction of blood volume occupied by red blood cells) and Y is the fractional oxygentation. Assuming that $\chi_{HbO} = \chi_{plasma} = \chi_{tissue} = \chi_{water} = 0$,

Eq.2.10 is reduced to:

$$\chi_{blood} = Hct\left((1-Y)\,\chi_{HbR}\right) \tag{2.11}$$

A change in oxygenation will result in a change in the susceptibility of blood:

$$\Delta\chi_{blood} = \Delta Y\, Hct \chi_{HbR} \tag{2.12}$$

Magnetic field inhomogeneities occur due to the presence of materials having different susceptibilities. The physical basis of the BOLD sensitivity of MR signal is that HbR alters the magnetic susceptibility of blood. At the onset of brain activation, the paramagnetic HbR creates a magnetic field gradient which shortens T_2 (free relaxation) and T_2^* (free induction decay) and reduces the MR signal [86, 87, 88]. However, brain activation leads to a much larger increase in blood flow than oxygen metabolism. Hence, the net oxygen extraction fraction drops with activation and the capillary and venous blood are more oxygenated. This means that there is less HbR present in the voxel. T_2^* becomes longer and the signal measured with T_2 and T_2^* weighted pulse sequence increases.

The effect of magnetic field inhomogeneities on transverse relaxation can be characterized by

$$R_2^* = R_2 + R_2^{'} \tag{2.13}$$

The relaxation rate R_2^* is the rate of free induction decay ($R_2^* = 1/T_2^*$) and contributes to the signal intensity of gradient-echo sequences. The relaxation rate R_2 ($R_2 = 1/T_2$) is the intrinsic tissue transverse relaxation rate and contributes to the signal intensity of spin-echo sequences. The relaxation rate $R_2^{'}$ is termed water resonance linewidth which is a measure of frequency distribution within a voxel [89]. The relative magnitude of $R_2^{'}$ is proportional to the susceptibility of magnetic field perturber as well as dimensions of the perturber relative to the local proton dynamics [90]. An approximate relationship between $R_2^{'}$ and blood properties can be described as follows:

$$R_2^{'} = \gamma B_0 V\, Hct\,(1-Y)\,\chi_{HbR} \tag{2.14}$$

where V is the resting venous volume fraction, Y is the fractional oxygenation, $Hct\,(1-Y)$ is the total amount of HbR, $B_0\chi_{HbR}$ is the size of the magnetic perturbation and γ is the gyromagnetic ratio. Hence, the decay rate $R_2^{'}$ is proportional to the total amount of HbR and V:

$$R_2^{'} \propto V\,[HbR] \tag{2.15}$$

To link the above expressions to MR signal, a simple model has been described for both spin-echo and gradient-echo sequences [80]. For a spin-echo sequence, the expression that relates proton density, T_1, T_2 and the MR signal is described as

$$S\,(T_E, T_R) = S_0\left(1 - 2e^{-(T_R - T_E/2)/T_1} + e^{-T_R/T_1}\right)e^{-T_E/T_2} \tag{2.16}$$

The signal intensity, $S\,(T_E, T_R)$, is dependent on T_E (the echo time) and T_R (the repetition time) of the experiment. S_0 is the proton density. At long $T_R$values, the expression reduces to:

$$S\,(T_E) = S_0 e^{-T_E/T_2} \tag{2.17}$$

Similarly, a gradient-echo planar imaging signal is also dependent on S_0, T_1 and T_2^*. In a gradient-echo sequence, the expression that relates these quantities to the MR signal is given by

$$S\,(T_E, T_R, \theta) = S_0 e^{-T_E/T_2^*}\frac{\left(1 - e^{-T_R/T_1} sin\theta\right)}{1 - e^{-T_R/T_1}e^{-T_R/T_2^*} - \left(e^{-T_R/T_1} - e^{-T_R/T_2^*}\right) cos\theta} \tag{2.18}$$

where θ is the flip angle. When $T_R \gg T_1$ and θ approaches to 0 (small flip angle), Eq. 2.18 reduces to

$$S\,(T_E) = S_0 e^{-T_E/T_2} \tag{2.19}$$

It is well known that when neural activity increases in a brain region, the local MR signal produced in that region increases by a small amount due to changes in blood oxygenation and the resulting alteration in local susceptibility. Figure 2.6 represents the TE dependence of the MR signal differences between active and resting state in the brain. Contrast between two signal intensities (S_{rest} and S_{active}) having a difference in

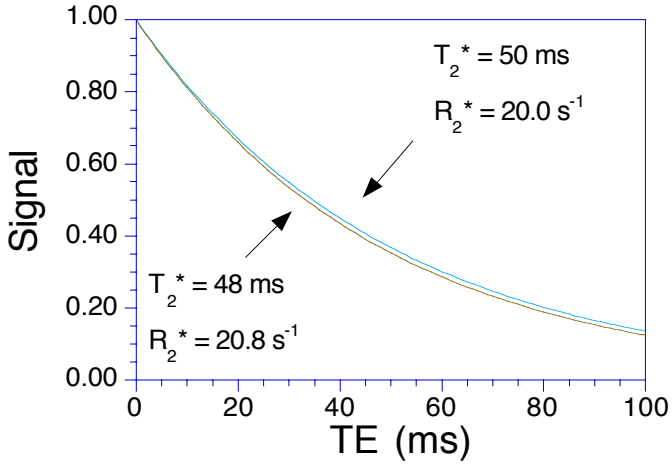

Figure 2.6 T_E dependence of the MR signal. The two curves represent typical values of R_2^* in the brain during rest (20.8 s^{-1}) and activation (20.0 s^{-1}). $S_0 = 1$. These signals are referred to as S_{rest} and S_{active} for resting and active brain respectively [90].

relaxation rate equal to ΔR_2^* (see Fig. 2.6), can be approximated as follows:

$$\Delta S = S_{active} - S_{rest} = S_0 e^{-R^*_{2active} T_E} - S_0 e^{-R^*_{2rest} T_E} \tag{2.20}$$

$$\Delta S = S_0 e^{-\left(R^*_{2rest} + \Delta R^*_2\right) T_E} - S_0 e^{-R^*_{2rest} T_E} = S_0 e^{-R^*_{2rest} T_E} \left(e^{-\left(\Delta R^*_2\right) T_E} - 1 \right) \tag{2.21}$$

where R^*_{2rest} is the relaxation rate associated with a measured S_{rest} at a given T_E value. For a small signal change, the measured fractional or percent signal change is given by

$$\frac{S_{active} - S_{rest}}{S_{rest}} = e^{-\Delta R^*_2 T_E} - 1 \approx -T_E \Delta R^*_2 \approx -T_E \gamma B_0 V Hct \left(1 - Y\right) \chi_{HbR} \tag{2.22}$$

This approximation forms the basis of the BOLD effect.

Over the last decade, fMRI has become a standard and indispensable tool in neuroscience research. Previously, positron emission tomography (PET) methods of measuring CBF change were the standard for mapping functional activity in the human brain. While PET studies are still done for a number of applications, most human brain mapping studies are now done with fMRI. In a typical fMRI experiment, the goal is to map patterns of neuronal activation in the subject's brain while he or she performs specific tasks. However, fMRI does not measure the neuronal activity itself.

Instead, the BOLD response to brain activation is sensitive to the concentration change of HbR, which in turn is dependent on cerebral blood flow (CBF), cerebral blood volume (CBV), and cerebral metabolic rate of oxygen ($CMRO_2$). A critical goal for interpreting fMRI data is to understand the underlying link between neuronal activity and the hemodynamic response. This is still an area of active research, and the reader is referred to the review by Uludag et al. [91] for an outline of the current thinking.

3. METHOD

3.1 Photon Migration in Biological Tissue

Near infrared imaging of the brain is based on measuring spatiotemporal variations in light absorption of the tissues between a source and a detector. Light is injected at the surface of the scalp, travels through extracerebral scattering tissues (i.e. scalp, skull and CSF) into the brain and again is received at the surface of the scalp. The photons emitted from the light source follow a statistical pattern and cross the scalp twice before being collected at the detector. In the wavelength range between 650 to 950 nm, the dominant absorbent chromophores are oxy- (HbO) and deoxyhemoglobin (HbR). Variations in the local concentrations of HbO and HbR (denoted as [HbO] and [HbR] respectively) modulate absorption properties of the brain in a wavelength dependent manner. The absorption coefficient at a given wavelength (λ) is linearly related to [HbO] and through [HbR] the equation:

$$\mu_a(\lambda) = \varepsilon_{HbO}(\lambda)[HbO] + \varepsilon_{HbR}(\lambda)[HbR] \tag{3.1}$$

where $\varepsilon_{HbO}(\lambda)$ and $\varepsilon_{HbR}(\lambda)$ denote wavelength dependent extinction coefficients of each chromophore [63]. A change in these chromophore concentrations due to brain activation alters the absorption coefficient and hence the detected light intensity. According to the modified Lambert-Beer law (MBLL), a small change in absorption coefficient is related to the change in measured optical density by the following formula:

$$\Delta OD(t,\lambda) = -log\left(\frac{\phi(t,\lambda)}{\phi_0(\lambda)}\right) = \Delta\mu_a(t,\lambda)\, L(\lambda) \tag{3.2}$$

where $\phi(t,\lambda)$ is the average intensity of the detected light, $\phi_0(\lambda)$ is the average intensity of incident light and $L(\lambda)$ is the effective average pathlength of light through the tissue [7, 92, 93, 94]. The effective pathlength is wavelength dependent but time-invariant when temporal absorption changes within the tissue are small. For a set of discrete volume elements (i.e. voxels) with each of them experiencing a different absorption

change, the MBLL can be formulated as follows:

$$\Delta OD\left(t,\lambda\right)=\sum_{j=1}^{Nvox}\mu_{a,j}\left(t,\lambda\right)L_{i,j}\left(\lambda\right) \tag{3.3}$$

where $L_{i,j}\left(\lambda\right)$ is the effective pathlength of light for the i^{th} measurement in the j^{th} voxel [7]. The spatial sensitivity profile of the photons can be determined with knowledge of the complex distribution of absorption and scattering properties of the tissues by empirical methods such as Monte Carlo based [95, 96, 97]. For each channel, Eq.**??** can be written in matrix form as

$$y\left(\lambda\right)=A\left(\lambda\right)\delta x\left(\lambda\right) \tag{3.4}$$

where y represents the time-series of optical signal changes with respect to baseline, $\delta x\left(\lambda\right)$ represents the changes in absorption coefficient for each voxel, and A is a three-point Green's function matrix which describes the linear transformation from absorption changes of the underlying media to the measured optical signal change at each channel. The A matrix can be referred to as the "photon absorption sensitivity profile" describing the spatial distribution of light traveling from a particular source to a detector [65], and usually has a "banana-shape" profile (a cross section of sensitivity profile is shown in Figure 2.3.

3.2 Subjects and Study Design

fMRI data were collected from 18 healthy subjects during a mental arithmetic task. 3 subjects were excluded due to excessive motion artefacts and the results for 15 healthy subjects will be shown here for analysis (ten male ages 28.4 $\pm$ 3 and five female ages 28 $\pm$ 3.2). The study was approved by the Ethics Committee of Boğaziçi University and written informed consents were obtained from all subjects after complete description of the study prior to the first session. During fMRI measurements; subjects were positioned supine and asked to refrain from excessive movements and stay motionless. Instructions about the protocol were given from a screen over the subject's

head. Each session started with a 30 seconds rest followed by a stimulation block of 39 seconds during which subjects were asked to serially subtract a 2 digit number from a 3 digit number (e.g., 146-84) and this block was followed by a 60 seconds of rest. This cycle was repeated 4 times. The arithmetic operations were displayed centrally in white color against a black background on a screen over the subjects' head. To avoid head movements, subjects were instructed to perform all tasks mentally, without vocalization nor any movement of body.

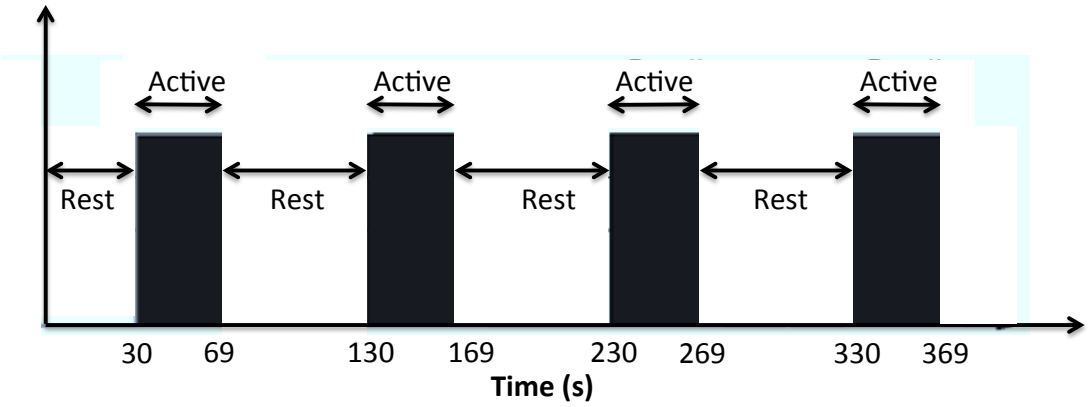

Figure 3.1 Schematic illustration of the stimulus timing. 4 consecutive blocks of mental arithmetic task were followed by a rest period of 60 seconds.

3.3 fMRI Data Acquisition

A Philips 1.5 T MR system (Philips Systems, Best, The Netherlands) was used to acquire T1- weighted images using a gradient echo planar imaging (EPI) sequence with repetition time (TR) = 3000 ms, echo time (TE) = 50ms, flip angle = 90 deg, matrix size = 64×64, 30 axial slices and voxel size = 3.59mm×3.59mm×2mm. Structural scans were also taken from each subject using a T1-weighted magnetization-prepared rapid acquisition gradient-echo (MPRAGE) sequence (0.9mm×0.9mm×1.2mm resolution) to perform segmentation and coregistration. A time series of 142 scans were collected for each subject. fMRI data processing was performed as follows: preprocessing steps consisting of motion and slice timing correction and temporal filtering

with linear trend removal were performed on functional scans using SPM8 software (www.fil.ion.ucl.ac.uk/spm, Wellcome Department of Imaging Neuroscience, UCL). The anatomical image was segmented into 5 tissue layers (gray matter (GM), white matter (WM), cerebrospinal fluid (CSF), skull and scalp) and the segmented layers were unified to form a new anatomical image onto which the functional image is coregistered.

The fNIRS probe (ARGES Cerebro, Hemosoft Inc, Turkey), for which we run photon migration simulations, contains 4 dual wavelength LED light sources and 10 photo-detectors arranged in a rectangular geometry. The sources and detectors are equidistantly placed on the probe with a nearest source-detector separation of 2.5 cm. Only SD pairs with minimum distance were considered resulting in 16 channels. During the fMRI measurements; we placed a sponge-like probe housing on each subject's forehead with all the LEDs and detectors removed and their positions replaced with vitamin E gel capsules to mark source and detector locations on the MRI images (See Figure 3.2).

3.4 Monte Carlo Simulations of Light Propagation in Extracerebral and Brain Tissue

The forward matrix **A** (Eq. 3.5), is a linear operator that translates absorption changes occurring at each volume element, to the measured optical signal between each SD pair. In our study; the **A** matrix is derived for each subject and channel and is used to estimate the contribution of hemodynamic changes occurring at each voxel to the total signal change observed at each particular SD pair. This forward model was formerly used to translate the hemodynamic changes observed within the fMRI space to the hemodynamic changes observed in the optical measurement space in a study by Huppert et al. [98].

We performed Monte Carlo simulations of light transport on subject-specific tis-

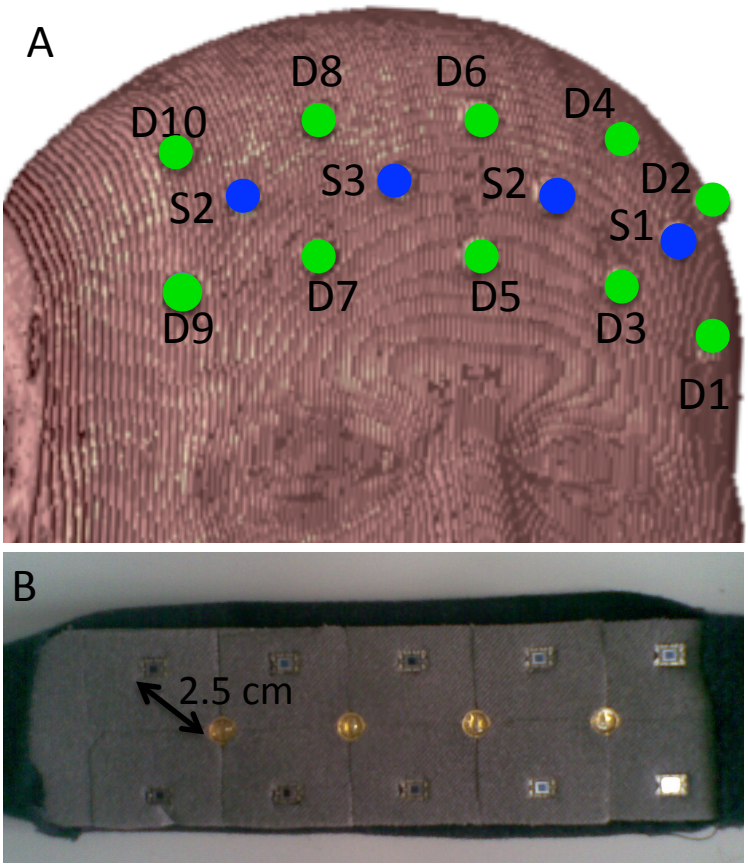

Figure 3.2 (A) Location of fNIRS source and detectors on the constructed anatomical image. (B) Probe design. The fNIRS probe (ARGES Cerebro, Hemosoft Inc., Turkey) for which we run photon migration simulations contains 4 dual wavelength LED light sources and 10 photo-detectors arranged in a rectangular geometry. The source and detectors are equidistantly placed on the probe with a source detector separation of 2.5 cm. During fMRI measurements; a sponge probe housing was placed on each subject's forehead with all the sources and detectors removed and their positions replaced with vitamin E gel capsules to mark source and detector locations on the MRI images.

sue segmented anatomical MR images with optical properties taken from Strangman et al. [63]. The absorption (μ_a) and scattering coefficients (μ_s) at 760 nm were taken as 0.0177/0.73 (scalp), 0.0125/0.93 (skull), 0.0021/0.01 (CSF), 0.0195/1.18 (GM), and 0.0195/1.18 mm (WM). Anisotropy factor (0.9) and refract index (1.4) were assumed to be the same in all segmented tissues. The simulations were run by the program named Monte Carlo eXtreme [99], provided to the public by the Photon Migration Imaging Laboratory at Massachusetts General Hospital (http://mcx.sourceforge.net/cgi-bin/index.cgi). To characterize absorption and scattering processes on realistic head models, source and detector positions were determined by identifying the location of vitamin E fiducial markers that were placed on the emptied spots of the fNIRS probe

A)

B)

Layer	$\mu_a(cm^{-1})$	$\mu_s(cm^{-1})$
Scalp	0.177	7.3
Skull	0.125	9.3
CSF	0.021	1
Gray Matter	0.195	11.8
White Matter	0.195	11.8

Figure 3.3 A) Anatomical MRI of a human head segmented into five tissue types (scalp, skull, cerebral spinal fluid, gray and white matter). B) Optical properties of the different tissue types chosen for the Monte Carlo simulations.

prior to the MPRAGE scans. After registering the locations of sources and detectors, Monte Carlo simulations of light transport were applied to the segmented anatomical head models generated for each subject and SD pair as described in Boas et al. [95]. The optical properties of white matter were set to those of gray matter due to the fact that changes in white matter properties have a negligible effect on the results [4]. For each source and detector position, the trajectories of 108 photons were simulated at 760 nm in order to predict the spatial distribution of light travelling from a source position to a detector position. The spatial sensitivity matrices were calculated only for the closest SD pairs. Figure 3.4 illustrates the spatial sensitivity profile of photon migration from a light source to a detector on an anatomical MRI image. The forward equation (Eq.3.5) sums voxel-wise changes in fMRI-BOLD signal over the volume using the weights of the sensitivity matrix **A** to predict the measurements between each source-detector pair.

3.5 fMRI Projection

The absolute BOLD signal intensity changes measured from each voxel are multiplied by the corresponding element of the optical forward matrix (**A**) projected onto

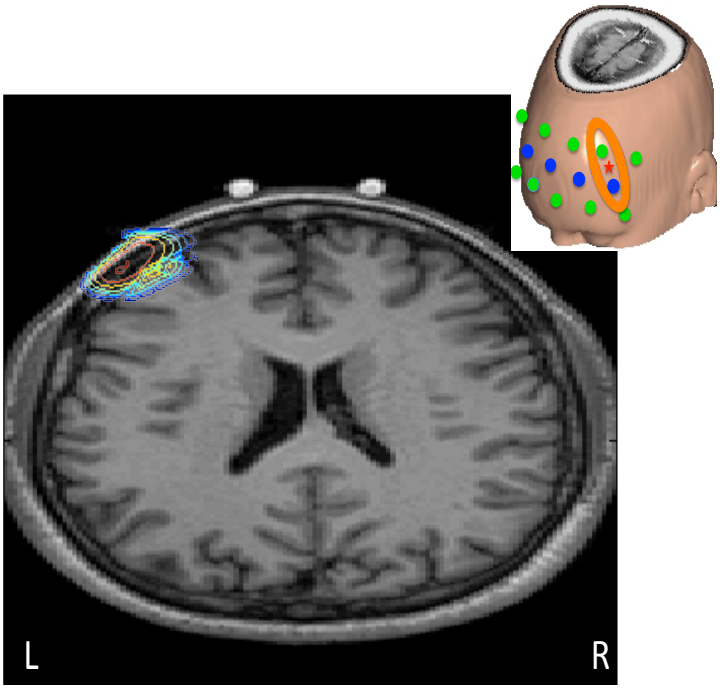

Figure 3.4 Photon absorption sensitivity profile for an SD pair separated by 2.5 cm. For each subject, first a 3D realistic head model is generated, then Monte Carlo simulations of light propagation are performed to obtain the spatial sensitivity profiles. The contour overlay is shown in logarithmic scale and contours are presented for each order of magnitude. The red star at the inset figure shows the location of this axial slice relative to the optical probe. The optically weighted Sum signal is obtained by multiplying BOLD activation at each voxel with the corresponding element of the sensitivity matrix **A**.

the functional space. This is established by registering the forward matrices obtained within the high resolution anatomical image space to the lower resolution functional image space. A mask with an intensity of 1 for voxels with an optical sensitivity greater than the threshold (taken as 60 dB signal loss of the maximum sensitivity) and zero elsewhere is formed for each SD pair. BOLD signals from voxels within the intersection of this mask and scalp tissue are scaled with the corresponding optical weight and their summation is denoted as optically weighted scalp BOLD signal under that SD pair. The same procedure with gray matter mask is followed to calculate the optically weighted brain BOLD signal. Although we report results using the Green's function at 760 nm, the results were nearly identical when optical properties at 690 and 830 nm were used.

3.6 Signal Model

Most neuroimaging techniques employ a standard analysis of functional brain activity signals with the assumption of a linear addition of hemodynamic changes (for further discussion, see [100]). BOLD signal from each SD pair contains the desired brain signal obscured by physiological noise. We will refer to the spatially and optically weighted BOLD signal for each SD pair as "Sum" signal and model it as:

$$Y_{Sum} = Y_{Brain} + Y_{Superficial} \tag{3.5}$$

We investigated the possibility that the brain signal can be further decomposed into two components: one related with task induced neural activation ("neural signal") and one reflecting the effects of global systemic physiology ("global signal") occuring in the brain. We modeled brain signal for each SD pair as

$$Y_{Brain} = Y_{Neural} + Y_{Global} \tag{3.6}$$

Hence, the physiological noise embedded in the Sum signal can be defined as

$$Y_{Noise} = Y_{Superficial} + Y_{Global} \tag{3.7}$$

Regressing the superficial and global components from the Sum signal for each SD pair should then, in principle, produce a more accurate measure of the task induced neural activation: $Y_{Sum} - Y_{Noise} = Y_{Neural}$[74]. As an example; the contribution of superficial noise regressor is removed by regression

$$Y_R = \alpha Y_{Sum} - Y_{Superficial} \tag{3.8}$$

where Y_R is the residual signal after noise removal and

$$\alpha = (Y_{Sum} \cdot Y_{Superficial})/(Y_{Superficial} \cdot Y_{Superficial}) \tag{3.9}$$

α is the scaling coefficient that minimizes the root mean square of Y_R [101]. For each SD pair, an optically and spatially weighted sum of BOLD absolute signal intensity changes taken from scalp voxels along the photon migration path are used to construct a

measure of hemodynamic changes localized to the superficial tissue layers ($Y_{Superficial}$) whereas an optically and spatially weighted sum of BOLD absolute signal intensity changes from brain voxels within the photon migration path are used to construct a measure of hemodynamic changes occurring in the brain (Y_{Brain}). We scale the optically weighted scalp BOLD signals with a proportionality constant of 4/5 taking into consideration the fact that i) BOLD signals obtained from the scalp mainly arise from intravascular signal changes, ii) they are affected in a more pronounced manner by the venous blood volume change rather than HbR concentration change and iii) at a magnetic field strength of 1.5 Tesla with $T_E = 50$ ms and assuming a venous oxygen saturation of 70%, the change in venous blood volume with activation is estimated to contribute with a weight of about 4/5 to the total BOLD signal change observed in the scalp tissue (The details of this estimation are given in Appendix C.). Prior to formation of the Sum signals, motion parameters obtained from the preprocessing step are regressed out from all scalp and brain signals for a fair test of the three regression methods.

For each subject and SD pair, we simulated a "short distance detector" placed close to the light source with a SD distance of approximately 1 cm. The position of each "short distance detector" was arranged to maximize the overlap between the corresponding 2.5 cm distance SD measurement and the simulated short distance channel measurement. We then defined a region of interest (ROI) in the scalp tissue beneath the short distance detector and the source for each simulated short distance channel. The fMRI signals extracted from the voxels in each scalp ROI were averaged and denoted as "superficial signals".

We attempt to quantify whether regressing the global or superficial signals alone is sufficient in retrieving the task induced neural signal. To explore the extent to which the Sum signal can be explained by the superficial signal, the Sum signals were regressed with the corresponding superficial signals for each subject. We call this method of eliminating superficial noise "superficial signal regression" (SSR). In the second method; we regressed out the global signal from every Sum signal and called this method "global signal regression" (GSR).

Last; we evaluate both SSR and GSR on Sum signals and name this method "extended superficial signal regression" (ESSR). The residual time series $v(t)$ can be obtained by,

$$Y_{Sum}(t) = [G(t) + S(t)]\beta + v(t) \tag{3.10}$$

where $Y_{Sum}(t)$ is the Sum data for a particular SD pair; $G(t)$ and $S(t)$ represent the global and superficial signals respectively, β is a vector of regression coefficients and $v(t)$ is the corresponding time series recovered after the global and superficial systemic signals are removed.

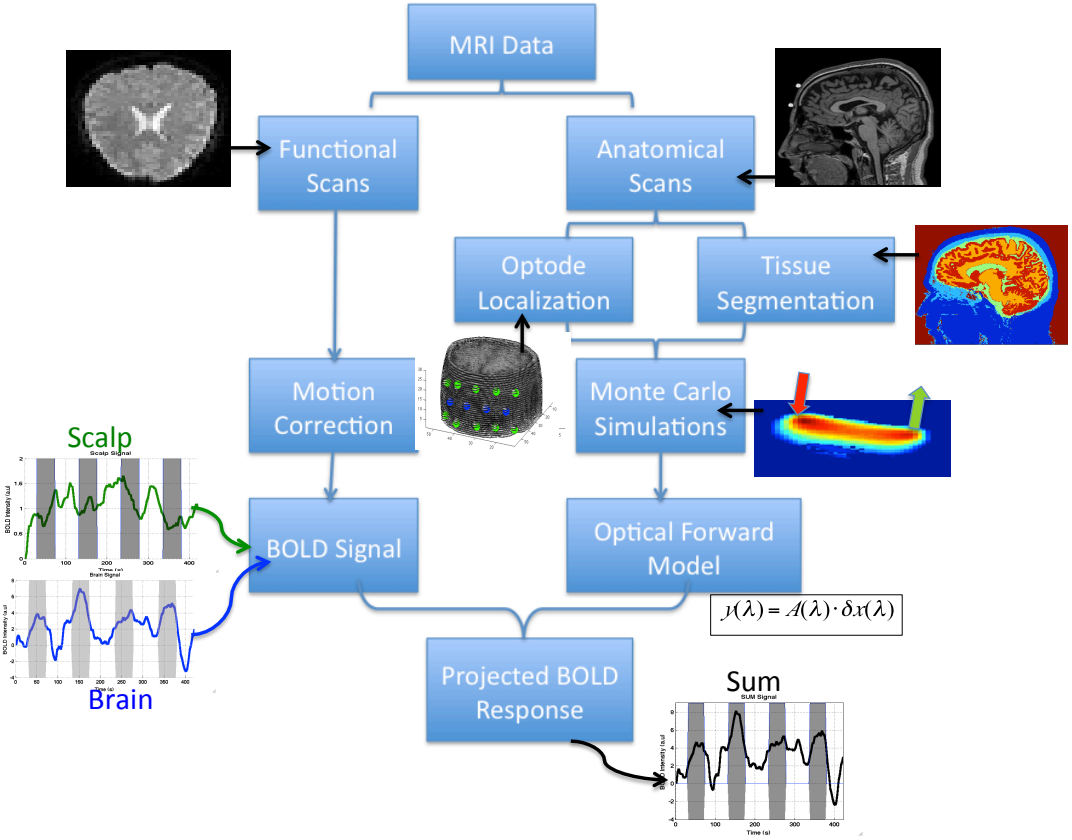

Figure 3.5 Processing steps for functional and anatomical data. The anatomical images are coregistered and segmented into a five-layered model (skin, skull, CSF and gray and white matter). This image is used to perform Monte Carlo simulations to determine the light propagation through the head. The sensitivity weights obtained for each voxel are then used to scale each voxel's data and sum them for gray matter and scalp masks separately.

3.7 Data Analysis

The performance of each regression method is determined by i) the Pearson correlation coefficient (R^2) and ii) the mean squared error (MSE) between task-related neural signal (neural) and the retrieved signal after each regression method. We also demonstrate the R^2 and MSE metrics between brain signal and the retrieved signals for comparison. The average of R^2 coefficients was calculated after applying the Fisher's r-to-z transformation and the resulting average is then back transformed [102]. R^2 coefficient shows how well the two signals co-vary independent of scale. Because this metric is not an indicator of how well the amplitude of the retrieved signal matches that of the neural signal, we also interpreted the MSE metrics.

To compare the quality of the signals retrieved after each regression method, we evaluated the contrast-to-noise ratio (CNR) of the retrieved hemodynamic response. Contrast is defined as the peak-height of response (averaged over multiple stimulus presentations). We characterized measurement noise through the standard deviation in the pre-stimulus baseline. We judged each method's effectiveness by its improvement in CNR with respect to original Sum signal. Percent CNR improvement ($\%CNR_{imp}$) is defined as

$$\%CNR_{imp} = 100 \times \frac{1 - CNR_A}{CNR_B} \tag{3.11}$$

where CNR_B represents CNR for original Sum signal and CNR_A is the CNR of the signal after the listed regression method is applied.

In addition, the variation among four activation blocks is measured by calculating coefficients of variation (CV), denoted as

$$CV = \frac{\sigma}{\mu} \tag{3.12}$$

where σ is the standard deviation across blocks and μ is the mean of each activation block.

We also investigated the effects of superficial noise and cerebral systemic physiology on the Sum signal by generating topographic maps of functional activation and analyzed their spatial patterns. The channel-wise hemodynamic responses during peak activation (taken as 14 seconds after stimulus onset) for each stimulus block are mapped onto forehead probe at the midpoint between each SD pair. The inverse distances calculated between each midpoint are used as weight factors to interpolate the peak responses over forehead. An image map is formed as shown in Figure 4.5. We quantified the resemblance of each method's map to the neural activation map by calculating the mean square error between images as

$$MSE_{Method} = \frac{1}{M} \cdot \frac{1}{N} \sum_{i=1}^{M} \sum_{j=1}^{N} \left(I_{Neural}^{i,j} - I_{Method}^{i,j} \right)^2 \tag{3.13}$$

where N is the number of activation blocks (4 in our experiments), M represents the number of subjects, $I_{Neural}^{i,j}$ represents the peak activation map obtained from neural signals for subject i and block j, and $I_{Method}^{i,j}$ represents the peak activation map obtained from the specified method for subject i and block j.

4. RESULTS

Figure 4.1 presents time traces of the hemodynamic response to the mental arithmetic task from a single representative SD pair before and after optically weighting the scalp and brain signals (Figure 4.1, panels A and B respectively). The optically weighted Sum signal for each SD pair is assumed to be the fMRI correlate of the corresponding fNIRS signal while the optically weighted brain and scalp signals represent the stimulus related brain functional response and overlying superficial scalp physiological fluctuations respectively. Notice how the scalp signal is enhanced in terms of magnitude and how the brain signal is obscured by it in the Sum signal after weighing BOLD data from voxels along the photon migration path with the sensitivity matrix (Figure 4.1, panels C and D). In Figure 4.2, we examine the effect of applying GSR, SSR and ESSR on retrieving the time traces of the evoked brain hemodynamic response. A representative case of applying GSR, SSR and ESSR is shown in Figure 4.2, panel B. The original Sum signal fails to show a canonical response (Figure 4.2, panel A) due to superficial and cerebral systemic interferences. When only global signal is removed (GSR), it is difficult to distinguish individual activation epochs whereas application of SSR or ESSR results in a consistent canonical hemodynamic response. Task-evoked activations are apparent even before block averaging when either SSR or ESSR method is used (Figure 4.2, panel B); however ESSR results in higher response amplitudes. Applying SSR or ESSR decreases block-to-block variation while improving signal quality (Figure 4.2, panel C) whereas with GSR only; it is difficult to observe task-evoked activation even in the block-averaged data. Block averaged ESSR data has improved statistical significance with more time points showing a significant rise relative to baseline (Figure 4.2, panel C. Asterisks mark sample points with a statistically significant deviation from prestimulus baseline of 5 seconds, $p<0.05$ with a two-tailed t-test.). In this representative measurement, GSR did not yield a significant improvement in the CNR or quality of the hemodynamic response. SSR improved CNR by 60% whereas ESSR resulted in a CNR improvement of 240%. These traces (Figure 4.2, panels B and C) show the ability of ESSR to reduce noise and increase statistical significance.

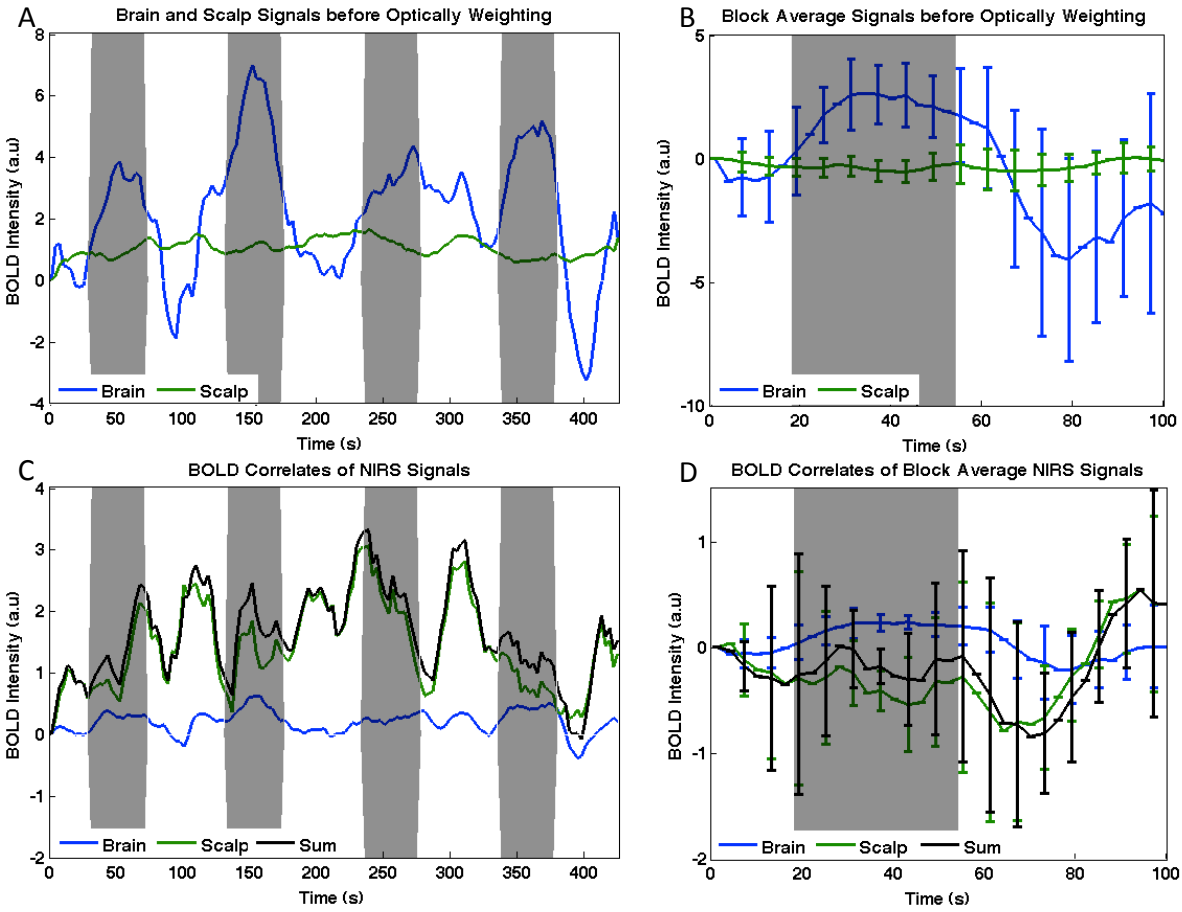

Figure 4.1 Temporal traces of brain and scalp BOLD signals for a single SD pair A) before C) after weighting with the optical sensitivity matrix. The scalp signal is highly correlated with the Sum signal (R^2= 0.92) while the brain signal is weakly correlated (R^2 = 0.35). B, D) Block averaged time traces of panels A and C respectively. Note how the brain BOLD signal is obscured in the Sum signal due to sensitivity preeminence of the scalp interference. Gray shaded regions indicate stimulus interval. The BOLD signal has arbitrary units.

The above-mentioned results can be generalized to the group data (N=240) demonstrating a consistent increase in CNR and decrease in coefficient of variability (CV) as global and superficial signals are removed consecutively (Figure 4.3). The CNR values obtained using the ESSR method are significantly higher than those obtained using the GSR and SSR methods (two-tailed paired t-test, $p<0.05$). Moreover; the CNR values obtained for the original Sum signals are significantly lower than the CNR values obtained using the SSR and ESSR methods (two-tailed paired t-test, $p<0.05$). The CNR values obtained with the GSR method do not demonstrate a statistically significant difference from the CNR values obtained for the original Sum signals (two-

tailed paired t-test, $p<0.05$). Similarly, CV values obtained using the ESSR method are significantly lower than those obtained with the GSR and SSR methods. Moreover; the CV values obtained for the original Sum signals are significantly higher than the CV values obtained using the ESSR method (two-tailed paired t-test, $p<0.05$). However no significance is observed between the CV values obtained using SSR and GSR methods.

Comparing % CNR improvement of the three methods shows that there are ameliorations in signal quality through the use of SSR or GSR alone, with SSR showing about 53% improvement while GSR results in an improvement of 24% among subjects showing positive improvement (Figure 4.4). There is a synergistic effect of utilizing both methods with the signal quality being highest after ESSR (60%). The % CNR improvements obtained for the original SSR and ESSR applied signals are significantly higher than the % CNR improvements obtained using the GSR method (two tailed paired t-test, $p<0.05$).

The summary of R^2 and MSE statistics over all subjects and measurements for each regression method are presented in Figures 4.5 and 4.6 respectively. Correlation of scalp, brain and neural signals with corresponding Sum signals and the retrieved signals after each regression method is shown in Figure 4.5.Without any of the regression methods applied; scalp and Sum signals are highly correlated (R^2=0.98, $p<0.05$) due to high sensitivity dominance of the scalp layer on the Sum signals. This finding is in accordance with a previous study by Takashi et al. who also showed a correlation of greater than 0.9 between near (5 mm) and far (30 mm) distance optical measurements which allowed them to probe skin, and a mixture of skin and brain measurements separately during a verbal fluency task [72]. After the global signal is removed; mean correlation between Sum and scalp signals decreases to 0.68. This result indicates that the recovered signals after GSR still contain a common effect with the superficial scalp signals and suggests that GSR is not sufficient for removing the entire physiological noise in the Sum signal. However; correlation between scalp signal and Sum signal decreases dramatically after regressing out the superficial scalp signal (Figure 4.5), which shows that the superficial signal regression method successfully extracts the

scalp interference from the Sum signal. For brain signals, the small but significant decrease in R^2 after global signal removal (0.29 to 0.25, $p<0.05$) may be due to the fact that we have achieved to cancel the global effect in the Sum signals while it is still buried in the brain signals. SSR applied Sum signals are highly correlated with the brain signals ($R^2=0.98$, $p<0.05$) whereas the correlation is slightly smaller when ESSR is applied ($R^2=0.96$, $p<0.05$). The small but significantly higher R^2 with SSR applied Sum signals may be due to the fact when only the superficial noise is removed, the effect of cerebral systemic physiology is still preserved in the remaining Sum signal which contributes to the correlation with brain signal. Instead; when both global and superficial noises are removed from the Sum signal (ESSR method); the brain signals contain a systemic effect while the ESSR applied Sum signals do not. This causes SSR applied Sum signals to have a higher correlation with brain signals than the ESSR applied Sum Signals ($R^2=0.98$ versus $R^2=0.96$ respectively, $p<0.05$ two tailed paired t-test). As the correlation between neural and Sum signals is analyzed; an increasing trend in R^2 is observed with application of GSR and SSR. Correlation between the neural and Sum signals reaches a maximum when ESSR is applied ($R^2=0.99$, $p<0.05$). This can be explained by the fact that when both superficial and global signals are removed from the Sum signal; the remaining signal better resembles the true task related neural activity, which is obtained by regressing out cerebral systemic effects from the brain signal.

The summary of MSE statistics over all subjects and measurements shown in Figure 4.6 prove that a significant improvement in signal quality and resemblance to neural signal are obtained after ESSR. The same MSE statistics is also shown for the brain signals for comparison. There is a significant decrease in the MSE between the neural signal and the Sum signal when SSR is applied and the MSE is lowest when ESSR is performed.

Figure 4.7 illustrates topographic images of a representative Sum signal (A), its scalp and brain components (B-C) as well as the Sum signal after GSR (D), SSR (E), ESSR (F) and the neural signal itself (G). Each column shows peak activation map from 4 consecutive stimulus blocks, for Sum (A), scalp (B), brain signals (C) and Sum

signal after GSR (D), Sum signal after SSR (E) and Sum signal after ESSR (F). The last column (G) illustrates activation map for the neural signal. Block average and image variance of the 4 stimulus blocks are illustrated below the block images. The Sum image is greatly influenced by the fluctuations at the scalp and shows inconsistent localization of the hemodynamic responses from block to block. It is difficult to observe the localized brain activity in the Sum signal due to high dominance of the superficial scalp layer fluctuations (Figure 4.7A, notice the variability among blocks 1-4) which tends to broaden some areas of activation while obscures some of them (compare second and third blocks of sum and brain images.) The brain map shows similar activations for each stimulus block, however the neural map presents a more localized pattern of activation (compare blocks 1-4 of Fig 4.5C and E). The ESSR images resemble the neural images most with the lowest mean square error. The mean square error (Eq. 3.13) for Sum, GSR, SSR and ESSR images are 0.55, 0.43, 0.025 and 0.008 respectively.

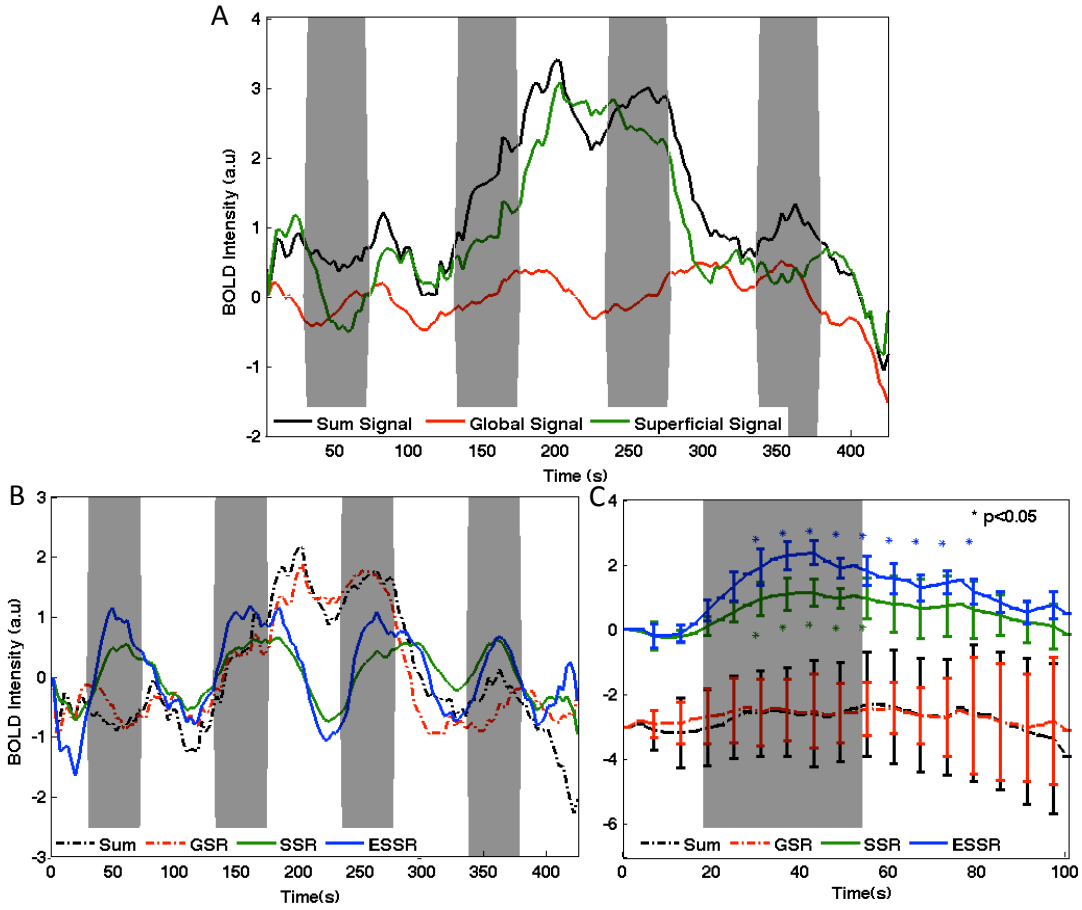

Figure 4.2 Evaluation of the effect of GSR, SSR and ESSR on a representative Sum signal. Time traces of the Sum, global and superficial signals from 4 consecutive stimulus blocks (gray shaded regions) are illustrated in panel A. B) Regressing out superficial noise signal from Sum signal produces SSR data whereas regressing out global noise signal produces GSR data. Regressing out both superficial and global signals produces ESSR data. C) Block averaged time traces of panel B). The shape of activation becomes cleaner with SSR and ESSR while applying GSR only does not produce a pronounced effect (Panels B and C). Error bars mark standard deviation and asterisks show statistically significant deviation from baseline (Panel C). Variation among 4 blocks decreases while CNR is enhanced after applying ESSR. Note the reduced standard deviation and improved number of sample points showing statistically significant rise after ESSR method when compared to SSR and GSR methods.

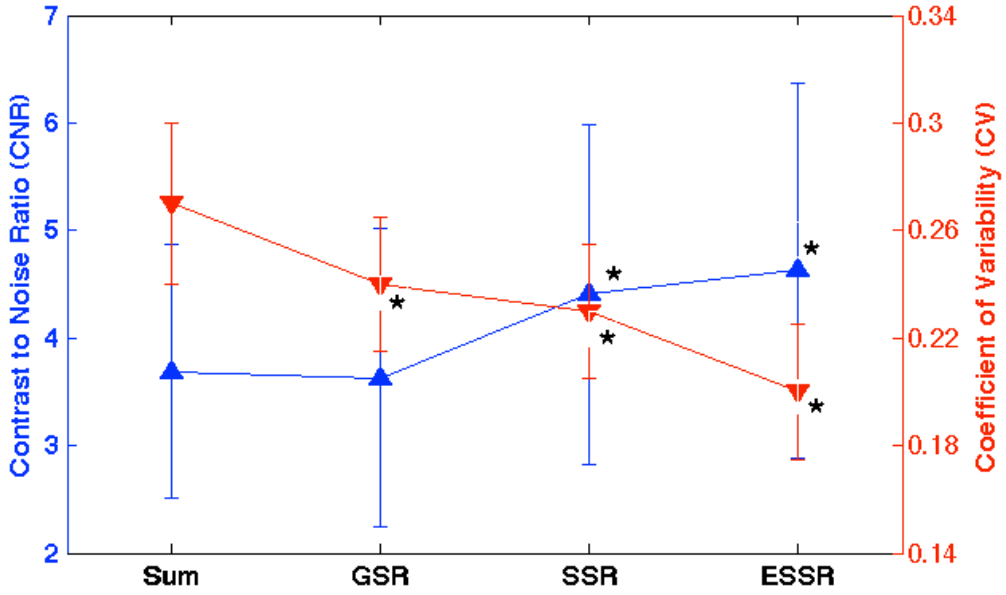

Figure 4.3 Grand average of the CNR and CV obtained for Sum Data and after GSR, SSR and ESSR are applied. The error bars show standard deviation across all measurements (N=240). Statistically significant differences from the Sum Data are marked with an asterisk (2 tailed paired t-test, $p<0.05$).

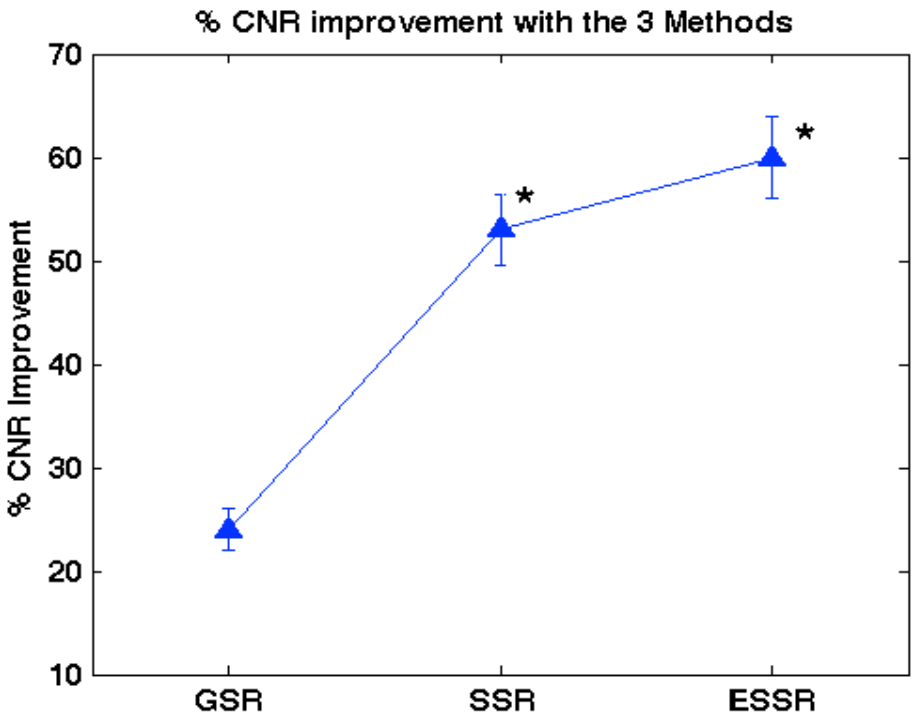

Figure 4.4 % CNR improvement observed relative to Sum Signal. The error bars show standard deviation across all measurements (N=240). Statistically significant differences from the Sum Data are marked with an asterisk (2 tailed paired t-test, $p<0.05$).

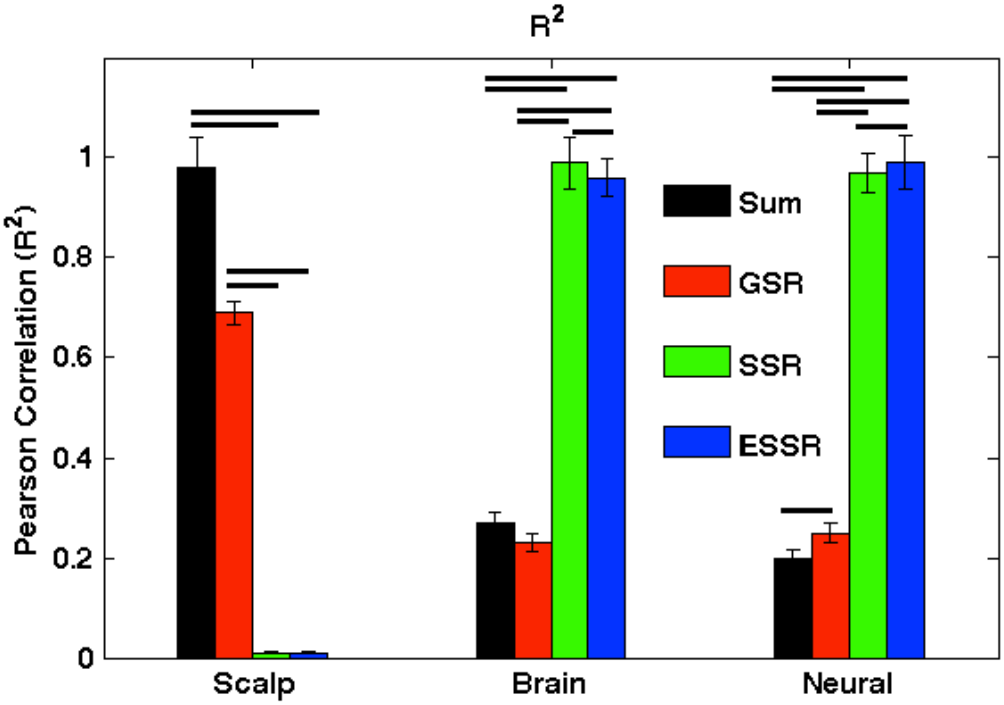

Figure 4.5 Correlation of scalp, brain and task induced neural activity related brain signal (neural) with Sum signal before performing any regression (Sum), after performing GSR, SSR and ESSR averaged for all subjects and measurements. Two tailed paired t-tests are performed between the R^2 computed for original Sum signals and the retrieved time series after each regression method. The bars represent the means of 240 measurements and the error bars represent standard error of the mean. Statistical significance at $p<0.05$ level are indicated by horizontal lines over the corresponding bars.

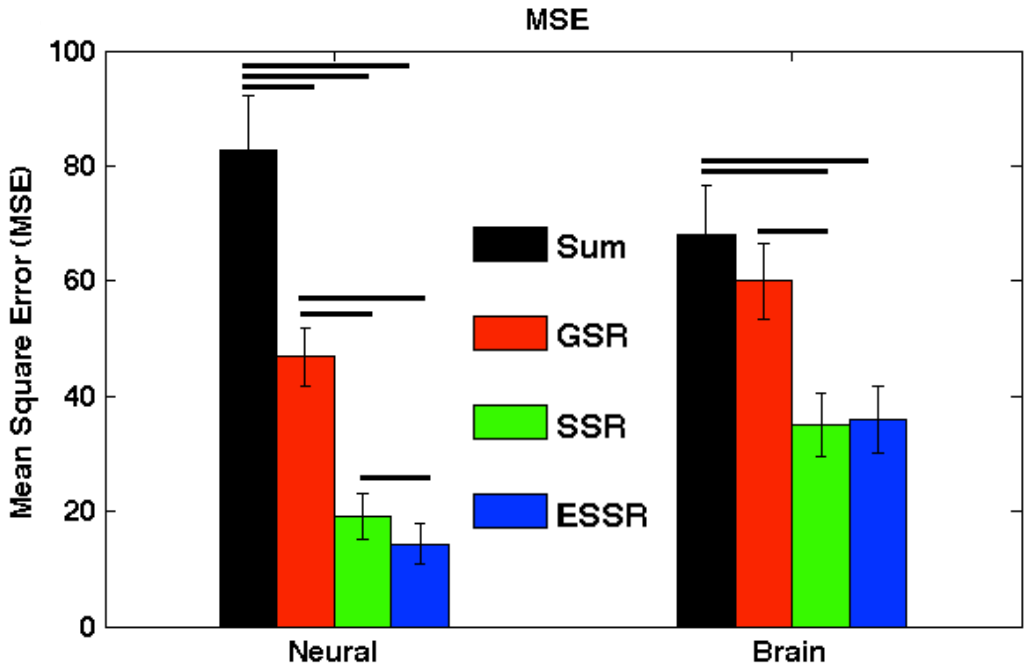

Figure 4.6 Mean Squared Errors (MSE) between the Sum signal and listed signals (neural and brain) before performing any regression on Sum signal, after performing GSR, SSR and ESSR. Two tailed paired t-tests are performed between the MSE computed for original Sum signal and the retrieved time series after each regression method. The bars represent the means of 240 measurements and the error bars represent standard error of the mean. Statistical significance at $p<0.05$ level are indicated by horizontal lines over the corresponding bars.

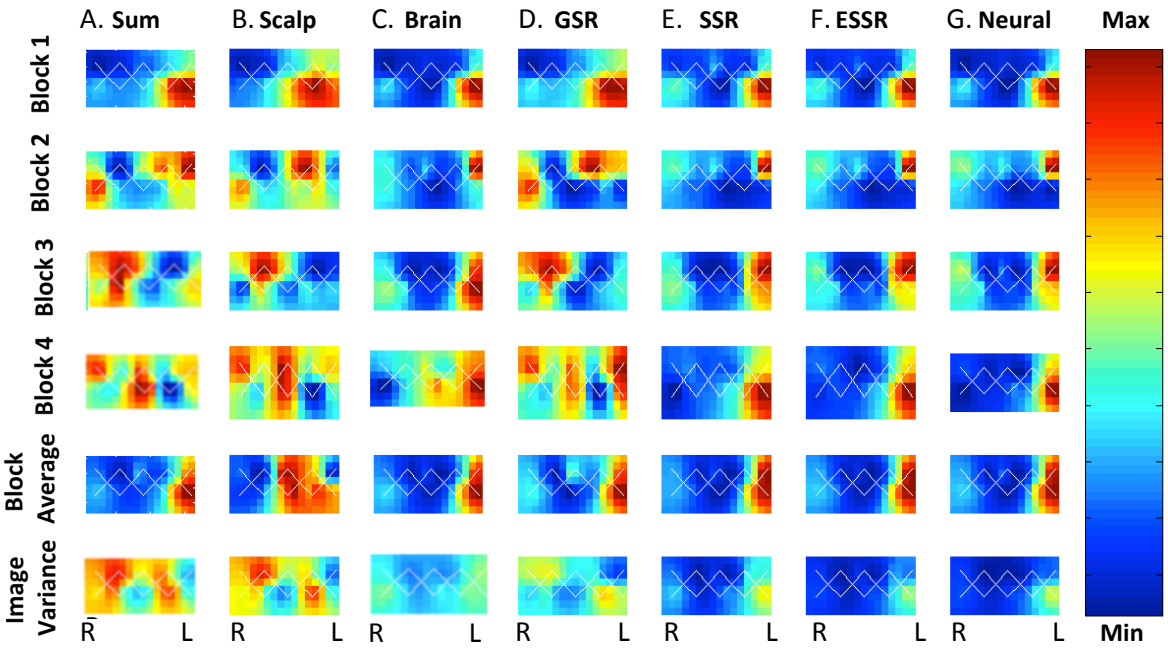

Figure 4.7 Evaluation of the effect of applying GSR, SSR and ESSR on image variance. Each column shows peak activation from 4 consecutive blocks, for (A) Sum, (B) scalp, (C) brain signals and (D) Sum signals after GSR, (E) Sum Data after GSR and (F) Sum Data after ESSR. The last column (G) illustrates activation map for the neural signal. Block average and image variance of the 4 stimulus blocks are illustrated below block images. Note how the block activations look similar after performing ESSR. Image variance is displayed as the standard deviation of each SD pair at peak activation across all blocks. Image variance plot captures very little inconsistency in ESSR data.

5. DISCUSSION

The major goal of our study is to compare the efficacy of removing physiological artifacts by performing i) a global signal regression (GSR), ii) a superficial signal regression (SSR) and iii) an extended superficial signal regression (ESSR) where both a simulated superficial scalp measurement and a global signal are regressed out from each SD pair BOLD signal. A second, yet more physiologically relevant and innovative goal is to prove that ESSR produces signals with a higher resemblance to the true task related neural activity.

We determined the relative efficacy and performance of systemic interference removal methods with a spatially weighted BOLD signal. This procedure has some advantages over simulated data and data collected in fNIRS settings. For simulated data; there is a high chance that the quality of conclusions depends on the compatibility of the model being used. The performance of most algorithms have some uncertainty as the exploited mathematical methods work with assumptions made on signal dynamics or underlying physiological mechanisms [103]. In an fNIRS setting, there is no access to an intact and uncorrupted brain signal because the brain signals are intermixed with the superficial physiological signals from the scalp. Unlike fNIRS, fMRI has the advantage of probing the brain tissue independent of the overlying scalp and skull layers. Signal from brain voxels is not mixed with superficial contamination but still is subject to cerebral systemic fluctuations interfering the brain's functional response. Superficial scalp BOLD signals collected from the overlap of the scalp mask with the photon sensitivity map contain physiological information from entire scalp tissue along the photon path. Hence, we investigated the effect of superficial contamination in a true setting in which we included physiological information from both where light is introduced and collected.

The fMRI-derived brain signals consist of a task-induced neural activation intermixed with the effects of cerebral systemic fluctuations. We assumed that this neural

activation signal is the "ground truth" for the desired task induced hemodynamic activity signal to be retrieved and quantify the performance and quality of each regression method by how well the retrieved signal resembles this ground truth neural signal. In the following; we will first briefly discuss the validity of our signal model and assess the improvements in signal quality and reproducibility of the results for the three methods. We will then provide some discussion about the physics and physiology of fMRI signals from the scalp and brain and the extent to which they can be used to quantify the fNIRS measurements obtained from both tissues.

5.1 Signal Model

Two types of physiological fluctuations might interfere with the neuronal activation patterns embedded in fNIRS recordings: spontaneous oscillations that are not necessarily task correlated and that can be systemic and brain driven; and systemic changes such as blood pressure increases that are phase locked to the task-evoked experiment. The well-known systemic physiological interference is caused by cardiac beat around 1 Hz, respiratory oscillations around 0.4 Hz and low frequency oscillations (LFOs). The suppression of cardiac pulsations and respiratory oscillations is relatively easy because the correlation between the interference and the functional response of brain functional activity is usually low. LFOs in cerebral hemodynamics occur in the range of 0.01-0.1 Hz and arise from two main sources: spontaneous changes in local vascular tone referred to as vasomotion and the global oscillations in arterial blood pressure known as Mayer waves [14] affecting both the scalp and brain signals. In addition to spontaneous oscillations, some types of stimuli may cause a systemic response (i.e. an alteration in cardiac rate, blood pressure or respiration frequency) which can result in a change in baseline scalp or cerebral blood flow that correlates with the stimulus period. Such task-related systemic changes that are locked and dependent to the type of activation have been extensively investigated by previous studies [68, 71, 70, 72, 104]. One option for uncoupling these systemic changes and the task-induced neural activation is acquiring multi-distance fNIRS measurements assuming that the short distance measurements predominantly reflect scalp hemodynamics. The

short distance measurement can then be removed from the long distance measurement, as performed in our simulations with the assumption that a similar superficial contribution is affecting both measurements [74, 101, 105]. Superficial signal regression methods have been reported to attenuate both global physiological and task evoked extracerebral hemodynamic changes in optical data [74, 105]. In the ESSR method, we accounted for systemic and task-evoked interferences separately with a global and a local scalp regressor and achieved an enhanced signal quality with higher CNR and better resemblance to the neural activity related component of the Sum signal when compared to the other two regression methods. The ESSR method also successfully reduced the inter-trial variability in the Sum signal which most probably stems from the underlying spontaneous activity as suggested by Fox and Raiche [106].

The physiological interference in fNIRS recordings can arise from the superficial scalp and skull tissue as well as the cerebral systemic oscillations in the brain tissue. Such physiological interference has been considered as a "global phenomenon" previously [74, 28, 29, 30, 33, 76, 32]. In contrast, we considered that the cerebral systemic oscillations have a global influence whereas the interference coming from superficial layers has a more pronounced localized effect on the fNIRS signals. Systemic oscillations affecting the brain are also present in the scalp tissue. Indeed, using long distance fNIRS measurements; Cooper et al. showed that low-frequency oscillations present in the fNIRS data correlated well with a large proportion of BOLD-fMRI voxels throughout the cortex [107]. They suggested that the majority of low frequency contribution to the fNIRS signals occurs in the superficial layers of the head and future studies exploiting the use of superficial measurements, as regressors will be more convenient for eliminating low frequency noise in the BOLD data. Frederick et al. also showed that the short distance fNIRS signals provided better noise removal from the BOLD data when compared to long distance fNIRS signals [108]. In accordance with these studies, we considered the simulated global and superficial scalp signals to be a good representation of the systemic interference common to both brain and scalp tissue as well as the more localized and dominant superficial physiological noise in the Sum signals. The cerebral systemic interference present in our measurements is modeled by averaging the scalp signals from all the simulated short SD pair locations in the

forehead. We assume the brain and scalp systemic variations to be correlated due to their close physiological and vascular connections as the heart, blood vessels, and lungs are the sources of the global pressure-induced oscillations, and the carotid artery is the common gateway for both scalp and brain hemodynamic oscillations [32]. Also it is known that diploic and emissary veins can enable blood exchange between the extra- and intracranial compartments of the forehead through the skull [109]. Therefore; we thought it is reasonable to take an average of all simulated scalp signals as a representative of global systemic physiology for each subject, which would attenuate variations common to all superficially sensitive channels and result in an enhanced waveform resembling the global interference in the brain. Similar approaches that used an average scalp regressor for removing global interference in the optical measurements were proposed previously in literature as well [74, 110].

5.2 Resemblance of the Retrieved Signals to the Task Related Neural Signal

Although the superficial scalp layer hemodynamic variations comprise a much larger portion of the total physiological interference due to sensitivity dominance of the scalp [111, 69], it is also necessary to account for the systemic physiological variations inherent in the brain when one attempts to retrieve the true neural activation in response to a task. A previous study by Huppert et al. noted the presence of a correlated temporal noise in concurrent fNIRS and cortical fMRI recordings and suggested that this noise did not originate from superficial scalp layer because their fMRI signals were obtained only from cortical tissues [34]. Such physiological fluctuations have been noted in other fMRI and optical imaging studies as well [11, 69, 112]. We therefore modeled the effect of cerebral systemic interference in the brain signals with an average scalp regressor (details are discussed in the previous section) and examined the effect of applying GSR, SSR and ESSR on retrieving the time traces of the hemodynamic changes associated with this "ground truth" signal resembling the desired neural activation (denoted as "neural signal").

First, we tested whether regressing an average scalp regressor would successfully extract all of the systemic effect present in both layers and named this procedure a "global signal regression" (GSR). From the changes in correlation between the scalp and Sum signal after GSR (Figure 4.5), we can conclude that GSR cannot filter all of the superficial contamination present in the Sum signal as the GSR applied Sum signals are still highly correlated with scalp signals (R^2=0.68, $p<0.05$). Moreover; the contrast to noise ratio is not enhanced significantly after GSR, and it is difficult to observe a canonical response in most of the measurements. Next, we tested the efficacy of removing the local superficial scalp signal from each measurement. We observed a substantial improvement in the signal quality as reflected in the CNR, R^2 and MSE metrics. When the superficial scalp signal is removed, the variation among blocks decreases (notice the decrease in CV in Figure 4.3A and the error bars in Figure 4.2C) to a better extent and it is easy to detect the canonical response at stimulus intervals for most of the measurements (an example is shown in Figure 4.2B) even before block averaging.

By comparing the effects produced by GSR and SSR alone; we conclude that superficial scalp signal contribution to fNIRS signals varies significantly among different regions in the forehead and a local measurement is necessary for cancelling the effects of superficial signal contamination adequately. A single global regressor did not contain the exact superficial noise information constrained to the overlying structures for each SD pair and was not able to recover the desired neural response accurately (note the MSE and R^2 statistics). This finding is in accordance with two recent studies which showed that the systemic interference in fNIRS measurements is not homogeneously distributed across the surface of the scalp [76] and the superficial task-evoked artifacts are more localized in the scalp draining veins [68]. For the neural signals, a small increase in R^2 is accompanied by a small decrease in MSE with GSR applied Sum signals (Figures 4.5 and 4.6). Instead; there is a sharp increase in R^2 and a sharp decrease in MSE for SSR applied Sum signals. These results also demonstrate that superficial layer interference is the major component of the total systemic interference that is in accordance with the simulation and human subject findings by Zhang et al. [32, 33].

In our study; we hypothesized that the cerebral systemic oscillations have a global effect whereas the superficial oscillations have a spatially heterogeneous effect. We accounted for both types of noise separately in the ESSR method and compared the retrieved signal with the neural signal that is considered to represent the "ground truth" brain activation free from cerebral systemic oscillations. The correlation between neural and ESSR applied Sum signals is highest while the MSE is smallest when compared to the other two methods. The signal quality is enhanced most when ESSR method is applied with decreased variation among stimulus blocks, a clear canonical waveform, highest CNR improvement and a better resemblance to the ground truth neural activation signal. Application of ESSR method improves signal quality, reduces inter-trial variability by effectively cancelling superficial scalp contamination as well as systemic interference inherent in the brain effectively. These improvements compared to GSR and SSR methods also suggest that our assumption of characterizing cerebral systemic physiology with the average of all scalp regressors is suitable for discarding the systemic components of the brain signal. The CNR and MSE metrics illustrate that we were able to recover the neural signal to a good extent. These results also show that ESSR method can reduce both spontaneous oscillations inherent in the brain and task-evoked extracranial effects during the mental arithmetic task.

5.3 Improvements in Activity Localization

We also investigated the effects of superficial noise and cerebral systemic physiology on the Sum signal by generating topographic maps of functional activation and their spatial patterns. We assessed the improvements in activation localization with the application of the above mentioned regression methods. The sum image is greatly influenced by the fluctuations at the scalp and shows inconsistent responses from block to block due to high dominance of the superficial scalp layer fluctuations (Figure 4.2A, notice the variability among blocks 1-4). The effects of global and superficial systemic interference tend to blur the areas of activation (Figure 4.7A). Such superficial scalp effects have been shown to worsen the signal-to-noise ratio, or be incorrectly interpreted as cerebral hemodynamic changes, resulting in false positives in fNIRS experiments

previously as well [68, 71, 70, 72].

The brain map shows similar activation patterns for each block. However; the neural map presents a more localized pattern of activation (compare blocks 1-4 of Figure 4.7C and E). This improvement in localization of activity is most probably due to the cancellation of the global noise buried in the brain. Applying ESSR method reduces the effect of both the superficial scalp fluctuations and cerebral systemic physiology and gives rise to maps that very well resemble the neural maps. Although all activation maps appear similar after block-averaging (fifth row of Figure 4.7), the greater noise in the Sum and scalp signals can be easily reflected in an image of variance map over multiple trials (sixth row of Figure 4.7).

5.4 Comparison with Other Methods

In our study, we have implemented a computationally simple regression procedure for removing the effects of global and superficial interference during a cognitive task. Our work provides complementary information to previous fNIRS studies, which tested the efficacy of adaptive filtering and linear regression of scalp measurements during visual activation [74, 31, 77]. Although adaptive filtering is a more powerful method than linear regression; Zhang et al. observed a mean improvement of 60% for 71% of their HbO_2 measurements and no CNR improvements were observed for HbR [77]. Similarly, Saager et al. reported that 75% of the channels showed a CNR improvement [73] while Gregg et al. observed an improvement of about 200% in CNR across all hemoglobin species in more than 80% of their subjects with linear regression [74]. In our study; we observed a positive improvement in CNR for 62% of our measurements with a mean improvement of 60% with ESSR. The amplitude of the cerebral hemodynamic response in the prefrontal cortex during a cognitive stimulation may be smaller when compared to hemodynamic responses obtained from primary sensory or motor cortex during activation [68]. For this reason, the CNR improvement obtained in our study may be smaller when compared to the CNR improvements observed during motor or visual stimulation in previous studies. Stimulus correlated systemic changes

(e.g., increase in cardiac rate, arterial blood pressure, respiration frequency), can induce a false positive effect on CNR and regressing it out may result in an impairment of the CNR. Potential reasons behind the lower CNR improvement should be investigated in detail. Comparable performance of the ESSR method suggests that effective filtering can be obtained with simple, easily implemented algorithms.

The acceptance of fNIRS in clinical applications requires the delivery of reliable and robust signals from a greater percentage of subjects included in the studies. By cancelling the effects of global and superficial systemic physiology, shorter studies with increased signal quality can be conducted on a greater number of subjects while the effects of fatigue and adaptation are minimized.

5.5 Physics and Physiology of Brain and Scalp fMRI Signals and Their Relation to Tissue Absorbance measured with fNIRS

Although our study relies on the similarity between fMRI and fNIRS signal changes observed during cognitive stimulation, there are several points to be considered when signals from the scalp and from the brain are compared for both modalities. fMRI signals from the brain have been shown to be sensitive to similar underlying hemodynamic changes with fNIRS signals [11, 113]. However; regarding fMRI signals from the scalp, neither the biophysical origin nor how they can be related to scalp optical signals have been well-investigated. In the following, we will discuss the physics and physiology of fMRI signals from the scalp and brain and how they can be related to temporal evolution of tissue oxygenation changes measured with fNIRS.

The most established theories of fMRI attribute the physiological origin of the BOLD signal to changes in local HbR content and blood volume [114, 115, 116]. The amplitude S of a single voxel MRI signal obtained with a gradient echo sequence with

echo time T_E can be related to tissue water content M_v and relaxation rate (T_2^*) as

$$S = M_v \cdot \left(\frac{-T_E}{T_2^*} \right) \tag{5.1}$$

There exists some fundamental differences when the theoretical frameworks used for interpreting brain and scalp fMRI signals are considered. The BOLD effect in the brain mainly arises from changes in local [HbR] which is reflected in venous blood relaxation time T_2^*. In contrast, the scalp fMRI signals are thought to be primarily determined by venous blood volume M_v in a voxel. At 1.5 T field strength, while the extravascular contribution to the brain fMRI signals is responsible for half of the signal change [84], the extravascular contribution to the scalp fMRI signals can be neglected due to low signal intensity. Therefore task-related changes observed in the scalp fMRI signal reflect intravascular changes which may originate from a change in venous blood oxygenation and the related change in blood relaxation time T_2 or a change in venous water volume M_v or a combination of both [68]. At a magnetic field strength of 1.5 Tesla with $T_E = 50$ ms and assuming a venous oxygen saturation of 70 %, the relative contribution of these biophysical mechanisms to the fractional BOLD signal change induced by activation can be estimated with the integrated model proposed by Uludag et al. [117] as

$$\frac{\Delta S}{S} = 1.26 \frac{\Delta \sum HbO}{\sum HbO + \sum HbR} + 0.4 \frac{\Delta \sum HbR}{\sum HbO + \sum HbR} \tag{5.2}$$

where S is the venous MRI signal, $\sum HbO$ and $\sum HbR$ represent the baseline amounts of HbO and HbR, respectively, and ΔS , $\Delta \sum HbO$ and $\Delta \sum HbR$ represent the task-related changes of each quantity with respect to baseline. The reader is referred to Appendix B for the derivation of Eq. 5.1 and Eq. 5.2 and details of the underlying assumptions. Eq. 5.2 shows that for a single voxel scalp fMRI signal, changes in HbO content contribute with a weighting factor of 1.26, while changes in HbR content contribute with a weighting factor that is three times smaller. Kirilina et al. showed that, the scalp fMRI signals obtained during different cognitive tasks were highly correlated with scalp HbO concentration changes whereas they exhibited no significant correlation with HbR [68]. Similarly, with simultaneous fNIRS and laser Doppler flowmetry recordings, Takahashi et al. demonstrated that blood flow and volume increased in the

forehead scalp during performance of a verbal fluency task [72]. However; no significant change in scalp HbR concentration was observed. The relative concentration changes of HbO and HbR measured by fNIRS correspond to the total change of $\Delta \sum HbO$ and $\Delta \sum HbR$ in the cutaneous veins which influence the fMRI signal according to Eq. 5.2. The fNIRS results obtained by the above-mentioned two former studies let us assume that for the scalp compartment $\Delta \sum HbR \approx 0$. Thus, the second term in Eq. 5.2 can be neglected and the venous volume change is reduced to $\frac{\Delta \sum HbO}{\Delta \sum HbO + \Delta \sum HbR}$. To sum up, we infer that i) the scalp fMRI signal is directly proportional to venous volume change and ii) venous volume change is reflected in the scalp fMRI signal with a scaling factor of 1.26. For example; a %5 increase in scalp fMRI signal corresponds to a venous blood volume to an increase of about %4.

5.6 Quantification of fNIRS Signals with a spatially weighted fMRI Signal

The fMRI-BOLD signal change originates primarily from the local concentration change of paramagnetic HbR molecules which results in an alteration of the magnetic susceptibility of blood and creates magnetic field inhomogeneities. Therefore, one would expect a correspondence between fNIRS-HbR and fMRI-BOLD signals. Numerous studies have been performed to explore correlations between fMRI and fNIRS signals both spatially and temporally [34, 35, 36, 38, 98]. Although most theoretical approaches suggest a strong correlation between HbR and BOLD, experimental validation is a controversial issue. Some studies reported a better temporal correspondence between HbO and BOLD signals [37, 118], while other studies have shown a better correspondence between HbR and BOLD signals [38, 119, 120]. This discrepancy in literature may be related to the differential sensitivity of BOLD signal to vascular compartments in presence of stronger or weaker static magnetic field [7, 121, 98]. Nonetheless; a synthesis of the results from these studies indicates that, there is a strong correspondence between signals measured with fNIRS and fMRI. By using the approach of BOLD signal projection through the optical sensitivity profile as performed in our

study, the spatial and temporal correlation between the fNIRS and fMRI measurements could be examined with strong statistical temporal and spatial correlation in previous studies [34, 35, 122]. Huppert et al. indeed showed that the fNIRS-HbR and BOLD activation patterns are qualitatively consistent with one another after projecting the BOLD absolute image intensity signal from each voxel coinciding the photon migration path through the forward matrix that was found by the Monte Carlo simulations [98]. Moreover; partial volume effects were avoided and the discrepancy in activation observed between fNIRS and fMRI recordings was corrected. Similarly; Sassaroli et al. found that a weighted average of the standard BOLD signal showed a strong spatial and temporal correlation with both HbO and HbR concentration changes measured with NIRS during a hand-tapping protocol [35]. These studies support the spatiotemporal correspondence hypothesized to exist between the brain component of the spatially weighted Sum signal and the fNIRS signals.

Relative changes of the fMRI signal contain at least two contributions: one resulting from the tissue blood volume changes and the second resulting from tissue oxygenation changes. The fMRI signal changes due to the first mechanism are expected to be positively correlated with sum of concentration changes of HbO and HbR as measured with fNIRS. Taking into consideration i) the fact that task evoked superficial signal changes in the forehead during cognitive tasks were observed for HbO but not HbR [68, 72], and ii) the striking similarity observed between the time courses of scalp fMRI and fNIRS HbO signals in a previous study [68]; we suggest that fMRI signal changes observed in the scalp for our study may better represent the NIRS HbO or total haemoglobin (HbT) signal. Attributing the scalp fMRI signal changes to blood volume change is in accordance with the study of Drummond who reported an increase in forehead scalp blood flow during mental arithmetic, and suggested that the vasodilation is mediated by a-adrenoceptors [123]. The scalp HbR content is expected to be less effected by the task since task performance should not influence the metabolic demand of scalp. Consequently, we suggest that task-related hemodynamic changes in the forehead scalp during the mental arithmetic task may be due to the vasodilation mechanism. Some previous NIRS studies demonstrated significant changes in HbO signal from prefrontal cortex during mental arithmetic tasks. Hoshi and Tamura

observed pronounced changes in HbO signal but not HbR during mental arithmetic in a 30-year-old male subject [124]. Similarly; in the work of Tanida et al.; mental arithmetic task caused increases in HbO and HbT concentration accompanied by a decrease in HbR in the right and left prefrontal cortices of all subjects [125]. These results suggest the brain component of the Sum signal might also better correlate with HbO or HbT changes measured with fNIRS. We therefore suggest that the spatially weighted Sum signal in our study may show better correspondence to the HbO or HbT signals measured with fNIRS.

5.7 Limitations of the Study and Recommendations for Future Work

One major limitation of our study is that we did not include any fNIRS measurements in the present work. Our analysis relies on a similarity between the time courses of fNIRS and fMRI signals instead of a quantitative comparison of the two modalities. Although the hemodynamic response measured with the two modalities might differ in terms of amplitude, the time course of the measured scalp hemodynamics has been shown to be very similar [68]. A quantitative analysis of concurrent fMRI and fNIRS scalp measurements can help us elucidate the effect of task-related scalp hemodynamics on long distance NIRS measurements and will be our objective for future studies.

The systemic physiological parameters, especially the power of LFOs measured during an fMRI session might differ compared to the same parameters obtained in a sitting position during an fNIRS session [126, 127]. In the sitting position, the power of LFOs in both the scalp and brain tissue will be higher than that during the supine position. However; the majority of the low- frequency contribution to the fNIRS signal will still be from the superficial tissue as discussed in previous studies [107, 128]. Further studies on how posture affects the performance of the ESSR method in an fNIRS setting are necessary although we believe it is reasonable to assume the superficial and global regressors obtained from the scalp measurements will still serve as a good mod-

eling waveform for physiological noise during both postures. One of the advantages of the ESSR method is its ease of use with any multi-distance fNIRS probe design, but this simplicity comes at the cost of making assumptions. One limitation is that there are likely several sources that contribute to the measured noise and that a multiple linear regression method combined with direct measurements of other systemic signals such as cardiac beat, breathing rate, and arterial blood pressure, may provide a better insight to understanding the effects of superficial and global interferences. Previous published work with 1.5 Tesla field strength has shown that fMRI and NIRS are sensitive to similar underlying hemodynamic changes [11, 113]. However, we should also note that fMRI signals obtained with 1.5 T MRI systems mainly reflect hemodynamic changes in venules and larger veins but not capillaries [129]. fMRI data collected at higher magnetic field strengths ($\geq$4 T) will improve the sensitivity to capillaries and accuracy of proposed method.

The ESSR method is chosen for examination of task-evoked neural activity during a cognitive task; care should be taken in choosing the appropriate noise removal method for each experiment. As noted earlier, alternative methods for modeling the systemic physiology based interference in fNIRS recordings have been proposed in the literature. Each method is based upon different assumptions about the systemic noise present in fNIRS signals. While we tested only 3 methods for a single type of cognitive stimulation, a detailed study testing which interference cancellation method works best for which type of stimuli will be a valuable future contribution.

6. CONCLUSION

In this dissertation, we have shown that treating superficial interference locally and cerebral interference globally with the ESSR method results in a more accurate recovery of the task-induced hemodynamic response with higher spatial localization and lower inter-trial variability when compared to the GSR and SSR methods. Using an average scalp regressor together with a local measure of superficial hemodynamics (ESSR method) better accounted for the systemic interference inherent in the brain. Our fMRI results demonstrate that i) superficial scalp interference is the major component of the total systemic interference and is not homogeneously distributed among different regions on the forehead, ii) optical measurements of the brain hemodynamics are greatly influenced by interference of superficial origin. We conclude that maximizing the overlap between the optical path of the superficial measurements and the longer distance measurements is of crucial importance for accurate recovery of the evoked hemodynamic response in fNIRS recordings. A short optode (probing local scalp hemodynamics) placed close to each source and detector would be, in principle, ideal for accurate recovery of the evoked hemodynamic response in fNIRS recordings at the expense of impracticality. Future studies are needed to design optimal multi-distance probe geometries that account for superficial interference properly with the least number of short optode measurements.

APPENDIX A. DERIVATION OF THE OPTICAL SENSITIVITY (A) MATRIX

Optical sensitivity (A) represents the change in optical density (OD) for a given source - detector pair (SD) with respect to a change in the absorption coefficient (μ_a) in a volume element (v)

$$A\left(SD, v\right) = \frac{\delta OD(SD)}{\delta v} \tag{A.1}$$

When changes in μ_a are small, sensitivity can be related to the mean partial path length (PPL) travelled by light within each volume element [40] as follows:

$$PPL\left(v\right) = \frac{\delta OD(SD)}{\delta \mu_a\left(v\right)} \tag{A.2}$$

Monte Carlo simulations are used to estimate the fluence Φ at the nodes (r) from the source (S) or detector (D). Establishing the equivalence of equations A.1 and A.2 with Monte Carlo fluence simulation requires the use of a sensitivity scaling factor [32]. The spatial sensitivity is calculated at r using the Rytov approximation

$$A\left(SD, r\right) = \frac{\Phi_S\left(r\right)\Phi_D\left(r\right)}{\Phi_S\left(r\right)} \tag{A.3}$$

The spatial sensitivity is then computed for each volume element $A\left(SD, v\right)$ by averaging the sensitivity at the constituent nodes. The mean optical path length (L) for each source-detector pair is calculated from the mean transit time (MTT) of photons estimated from the Monte Carlo simulation by

$$L(SD) = MTT(SD) \cdot c_t \tag{A.4}$$

where c_t is the speed of light in the tissue. The volumetric spatial sensitivity $A\left(SD, v\right)$ is then rescaled to establish equation A.2 by requiring that

$$\sum_v A\left(SD, v\right) = L\left(SD\right) \tag{A.5}$$

APPENDIX B. ANALYTICAL APPROXIMATION FOR THE LEAST-SQUARE COEFFICIENT

The two detector geometry allows the head to be modeled as a system of two homogeneous layers with different μ_a values. The simulated short distance (Y_{Short}) and long distance (Y_{Long}) measurement signals can be regarded as

$$Y_{Short}(t) = \Delta\mu_{a1}(t) \cdot \langle L_1 \rangle_{Short} + \Delta\mu_{a2}(t) \cdot \langle L_2 \rangle_{Short} \tag{B.1}$$

and

$$Y_{Long}(t) = \Delta\mu_{a1}(t) \cdot \langle L_1 \rangle_{Long} + \Delta\mu_{a2}(t) \cdot \langle L_2 \rangle_{Long} \tag{B.2}$$

where the subscripts 1 and 2 refer to upper (scalp) and lower (brain) layers respectively. Following the work of Fabbri et al. [130], all influence of $\Delta\mu_{a1}(t)$ can be removed from the time course of Y_{Long} by subtracting a multiple of Y_{Short}:

$$R(t) = Y_{Long}(t) - K \cdot Y_{Short}(t) \tag{B.3}$$

which yields

$$R(t) = \Delta\mu_{a1}(t)(\langle L_1 \rangle_{Long} - K \cdot \langle L_1 \rangle_{Short}) + \Delta\mu_{a2}(t) \cdot \Big(\langle L_2 \rangle_{Long} - K\langle L_2 \rangle_{Short}\Big) \tag{B.4}$$

By choosing

$$K = \frac{\langle L_1 \rangle_{Long}}{\langle L_1 \rangle_{Short}} \tag{B.5}$$

we can eliminate $\Delta\mu_{a1}(t)$.

Unfortunately, the ratio of the average path length traveled in the top layer by photons reaching short and long distance detectors cannot be calculated. A new method

of subtracting the two measurements to isolate useful information about hemodynamics in the lower, cerebral layer is proposed by computing a least squares fitting coefficient $Y_{Short}(t)$ to $Y_{Long}(t)$.

The changes in absorption in both layers can be parametrized in the following manner:

$$\Delta\mu_{a1} = \mathbf{G} \tag{B.6}$$

$$\Delta\mu_{a2} = \gamma\mathbf{G} + \mathbf{B} \tag{B.7}$$

where $\mathbf{B}$ (bottom) is an absorption time course that appears only in the lower layer and $\mathbf{G}$ (global) is another one that can appear in both layers with different magnitudes, depending on the scaling parameter. Here, $\mathbf{B}$ can be defined as the part of $\Delta\mu_{a2}$ uncorrelated with $\mathbf{G}$ in the limit of infinitely long measurement;

$$\lim_{t\to\infty} \frac{\mathbf{B}\cdot\mathbf{G}}{\mathbf{G}\cdot\mathbf{G}} = 0 \tag{B.8}$$

The goal of diffuse optical measurements is to extract not $\Delta\mu_{a2}$ (the total cerebral hemodynamic time course), but $\mathbf{B}$ (the signal that is intrinsic to the cerebral layer only). By including γ, we count for the possibility that the interfering trend, $\mathbf{G}$ need not be exclusively confined to the top layer but can be global in nature as well.

Fitting the short distance simulated fNIRS measurement to the long distance simulated fNIRS measurement by least-squares yields a fitting coefficient α_{LS} where by definition

$$\alpha_{LS} = \frac{Y_{Short}\cdot Y_{Long}}{Y_{Short}\cdot Y_{Short}} \tag{B.9}$$

Hence; the residual time series reflecting task-induced brain signal can be obtained by

$$Y_R = Y_{Long} - \alpha_{LS} Y_{Short} \tag{B.10}$$

APPENDIX C. DERIVATION OF SCALING FACTORS THAT DESCRIBE THE RELATIVE CONTRIBUTION OF HBO AND HBR CHANGES TO THE MRI SIGNAL

The amplitude S of an fMRI signal averaged over all voxels containing the cutaneous veins is determined by venous blood volume and venous blood relaxation time:

$$S \sim M_v \cdot exp\left(-\frac{T_E}{T_2^*}\right) \tag{C.1}$$

where M_v is the total amount of protons in the vein and $1/T_2^*$ is transverse relaxation rate resulting from the interaction of water protons with HbR molecules in the blood. M_v is proportional to the total blood volume hence, it is also proportional to the total amount of hemoglobin in the veins. Eq. C.1 can be reformulated as

$$S \sim \left(\sum HbO + \sum HbR\right) \cdot exp\left(-\frac{T_E}{T_2^*}\right) \tag{C.2}$$

where $\sum HbO$ and $\sum HbR$ are the total amount of the venous oxy and deoxyhemoglobin respectively. Uludag et al.[117] demonstrated the intravascular relaxation rate of blood water molecules diffusing in an inhomogeneous field by red blood cells can be described by the following relationship:

$$\frac{1}{T_{2,HbR}} = \frac{12.67}{Tesla^2 \cdot s} \cdot B_0^2 \cdot \left(\frac{\sum HbR}{\sum HbR + \sum HbO}\right)^2 \tag{C.3}$$

The relative amplitude of the fMRI signal changes can be calculated by inserting Eq.C.3 into Eq.C.2 and differenting it with respect to $\Delta \sum HbO$ and $\Delta \sum HbR$. The relative amplitude of the fMRI signal change is :

$$\frac{\Delta S}{S} = \left(\frac{\Delta \sum HbO}{\sum HbO + \sum HbR} + \frac{\Delta \sum HbR}{\sum HbO + \sum HbR}\right) + \frac{2T_E}{T_{2,Hb}}\left(\frac{\Delta \sum HbO}{\sum HbO + \sum HbR} - \frac{\sum HbO}{\sum HbR}\frac{\Delta \sum HbR}{\sum HbO + \sum HbR}\right) \quad \text{(C.4)}$$

where the term in the first brackets describes the fMRI signal changes induced by a change in venous volume and the term in the second bracket describes the signal changes due to the change in relaxation time induced by HbR concentration change. At a magnetic field strength of 1.5 Tesla with $T_E = 50$ ms and assuming a venous oxygen saturation of 70 %, Eq.C.4 can be re-rewritten as:

$$\frac{\Delta S}{S} = \left(\frac{\Delta \sum HbO}{\sum HbO + \sum HbR} + \frac{\Delta \sum HbR}{\sum HbO + \sum HbR}\right) + 0.26\left(\frac{\Delta \sum HbO}{\sum HbO + \sum HbR} - 2.3\frac{\Delta \sum HbR}{\sum HbO + \sum HbR}\right) \quad \text{(C.5)}$$

The scaling factors before the first and second brackets indicate that the venous volume change and changes in HbR concentration contribute to the fMRI signal change with weights of 4/5 and 1/5.

REFERENCES

1. Franceschini, M. A., and D. A. Boas, "Noninvasive measurement of neuronal activity with near-infrared optical imaging," *Neuroimage*, Vol. 21, pp. 372–386, 2004.

2. Gibson, A. P., J. C. Hebden, and S. R. Arridge, "Recent advances in diffuse optical imaging," *Phys. Med. Biol.*, Vol. 50, pp. R1–R43, 2005.

3. Obrig, H., and A. Villringer, "Beyond the visible- imaging the human brain with light," *Cereb. Blood Flow Metab.*, Vol. 23, pp. 1–18, 2003.

4. Boas, D., and A. M. Dale, "Simulation study of magnetic resonance imaging-guided cortically constrained diffuse optical tomography of human brain function," *Applied Optics*, Vol. 44, pp. 1957–1968, April 2005.

5. Lloyd-Fox, S., A. Blasi, and C. E. Elwell, "Illuminating the developing brain: the past, present and future of functional near infrared spectroscopy," *Neurosci. Biobehav. Rev.*, Vol. 34, pp. 269–284, February 2010.

6. May, L., K. Byers-Heinlein, J. Gervain, and J. F. Werker, "Language and the newborn brain: Does prenatal language experience shape the neonate neural response to speech?," *Frontiers in Language Sciences*, Vol. 34, pp. 269–284, February 2011.

7. Boas, D., A. M. Dale, and M. A. Franceschini, "Diffuse optical imaging of brain activation: approaches to optimizing image sensitivity, resolution and accuracy," *Neuroimage*, Vol. 23, no. 10, pp. S275–S288, 2004.

8. Villringer, A., and B. Chance, "Non-invasive optical spectroscopy and imaging of human brain function," *Trends Neurosci.*, Vol. 20, pp. 435–442, 1997.

9. Obrig, H., M. Neufang, M. Wenzel, R. Kohl, M. Steinbrink, J. E. haupl, and A. Villringer, "Spontaneous low frequency oscillations of cerebral hemodynamics and metabolism in human adults," *Neuroimage*, Vol. 12, no. 6, pp. 623–639, 2000.

10. Payne, S., and J. S. abd D. A. Boas, "Effects of autoregulation and co2 reactivity on cerebral oxygen transport," *Ann. Biomed. Eng.*, Vol. 37, no. 11, pp. 2288–2298, 2009.

11. Toronov, V., M. Franceschini, M. Filiaci, S. Fantini, M. Wolf, A. Michalos, and E. Gratton, "Near-infrared study of fluctuations in cerebral hemodynamics during rest and motor stimulation: temporal analysis and spatial mapping," *Med. Phys.*, Vol. 27, no. 4, pp. 801–815, 2000.

12. Gustafsson, H., "Vasomotion and underlying mechanisms in small arteries. an in vitro study of rat blood vessels," *Acta. Physiol. Scand.*, Vol. 614, pp. 1–44, 1993.

13. Mayhew, J. E. W., S. Askew, Y. Zheng, J. Porril, G. W. M. Westby, P. Redgrave, D. M. Rector, and R. M. Harper, "Cerebral vasomotion: A 0.1-hz oscillation in reflected light imaging of neural activity," *Neuroimage*, Vol. 4, pp. 183–193, 1996.

14. Julien, C., "The enigma of mayer waves: facts and models," *Cardiovasc. Res.*, Vol. 70, pp. 12–21, 2006.

15. Zhang, R., J. H. Zuckerman, K. Iwasaki, T. E. Wilson, C. G. Crandall, and B. D. Levine, "Autonomic neural control of dynamic cerebral autoregulation in humans," *Circulation*, Vol. 106, no. 14, pp. 1814–1820, 2002.

16. Franceschini, M., S. Fantini, J. Thompson, J. Culver, and D. Boas, "Hemodynamic evoked response of the sensorimotor cortex measured noninvasively with near-infrared optical imaging," *Psychophysiology*, Vol. 40, no. 4, pp. 548–560, 2003.

17. Jasdzewski, G., G. Strangman, J. Wagner, K. K. Kwong, R. A. Poldorack, and D. A. Boas, "Differences in the hemodynamic response to event-related motor and visual paradigms as measured by near-infrared spectroscopy," *Neuroimage*, Vol. 20, no. 1, pp. 479–488, 2003.

18. Jasdzewski, G., G. Strangman, J. Wagner, K. K. Kwong, R. A. Poldorack, and D. A. Boas, "Differences in the hemodynamic response to event-related motor and visual paradigms as measured by near-infrared spectroscopy," *Neuroimage*, Vol. 20, no. 1, pp. 479–488, 2003.

19. Diamond, S. G., T. J. Huppert, V. Kolehmainen, M. A. Franceschini, J. P. Kaipio, and S. R. Arridge, "Dynamic physiological modeling for functional diffuse optical tomography," *Neuroimage*, Vol. 30, pp. 88–101, 2006.

20. Kolehmainen, V., S. Prince, S. R. Arridge, and J. P. Kaipio, "State-estimation approach to the nonstationary optical tomography problem," *J. Opt. Soc. Am. A Opt Image Sci Vis*, Vol. 20, pp. 876–889, 2003.

21. Prince, S., V. Kolehmainen, J. P. Kaipio, M. A. Franceschini, D. Boas, and S. R. Arridge, "Time-series estimation of biological factors in optical diffusion tomography," *Phys. Med. Biol.*, Vol. 48, pp. 1491–1504, 2003.

22. Prince, S., V. Kolehmainen, J. P. Kaipio, M. A. Franceschini, D. Boas, and S. R. Arridge, "Wavelet minimum description length detrending for near-infrared spectroscopy," *J. Biomed. Opt.*, Vol. 14, no. 3, pp. 034004–034004–13, 2009.

23. Lina, J. M., M. Dehaes, C. Matteau-Pelletier, and F. Lesage, "Complex wavelets applied to diffuse optical spectroscopy for brain activity detection," *Opt. Express*, Vol. 16, no. 2, pp. 1029–1050, 2008.

24. Lina, J. M., C. Matteau-Pelletier, M. Dehaes, , M. Desjardins, and F. Lesage, "Wavelet-based estimation of the hemodynamic responses in diffuse optical imaging," *Med. Image Anal.*, Vol. 14, pp. 606–616, 2010.

25. Matteau-Pelletier, C., M. Dehaes, F. Lesage, and J. M. Lina, "1/f noise in diffuse optical imaging and wavelet-based response estimation," *IEEE Trans. Med. Imaging*, Vol. 28, pp. 415–422, 2009.

26. Franceschini, M., D. K. Joseph, T. J. Huppert, S. G. Diamond, and D. Boas, "Diffuse optical imaging of the whole head," *J. Biomed. Opt*, Vol. 11, no. 5, pp. 054007–054007–10, 2006.

27. Zhang, Q., D. H. Brooks, M. A. Franceschini, and D. A. Boas, "Eigenvector-based spatial filtering for reduction of physiological interference in diffuse optical imaging," *J. Biomed. Opt*, Vol. 10, no. 1, pp. 011014–011014–11, 2005.

28. Umeyama, S., and T. Yamada, "New method of estimating wavelength-dependent optical path length ratios for oxy- and deoxyhemoglobin measurement using near-infrared spectroscopy," *J. Biomed. Opt*, Vol. 14, no. 5, pp. 054038–054038–6, 2009.

29. Umeyama, S., and T. Yamada, "Monte carlo study of global interference cancellation by multidistance measurement of near-infrared spectroscopy," *J. Biomed. Opt*, Vol. 14, no. 6, pp. 064025–064025–10, 2009.

30. Yamada, T., S. Umeyama, and K. Matsuda, "Multidistance probe arrangement to eliminate artifacts in functional near-infrared spectroscopy," *J. Biomed. Opt*, Vol. 16, no. 4, pp. 717420–717420–9, 2009.

31. Saager, R. B., and A. J. Berger, "Direct characterization and removal of interfering absorption trends in two-layer turbid media," *J. Opt. Soc. Am. A*, Vol. 22, no. 9, pp. 1874–1882, 2005.

32. Zhang, Q., E. Brown, and G. Strangman, "Adaptive filtering for global interference cancellation and real-time recovery of evoked brain activity: A monte carlo simulation study," *J. Biomed. Opt.*, Vol. 12, no. 4, pp. 044014–044014–12, 2007.

33. Zhang, Q., E. Brown, and G. Strangman, "Adaptive filtering to reduce global interference in evoked brain activity detection: A human subject case study," *J. Biomed. Opt.*, Vol. 12, no. 6, pp. 064009–064009–12, 2007.

34. Huppert, T. J., R. D. Hoge, S. G. Diamond, M. A. Franceschini, and D. A. Boas, "A temporal comparison of bold, asl, and nirs hemodynamic responses to motor stimuli in adult humans," *Neuroimage*, Vol. 29, no. 2, pp. 368–382, 2006.

35. Sassaroli, A., F. B. de Blaise, Y. Tong, P. F. Renshaw, and S. Fantini, "Spatially weighted bold signal for comparison of functional magnetic resonance imaging and near-infrared imaging of the brain," *Neuroimage*, Vol. 3, no. 2, pp. 505–514, 2006.

36. Steinbrink, J., A. Villringer, F. Kempf, D. Haux, S. Boden, and H. Obrig, "Illuminating the bold signal: combined fmri-fnirs studies," *Magn. Reson. Imaging*, Vol. 24, pp. 495–505, 2006.

37. Strangman, G., J. P. Culver, J. H. Thompson, and D. A. Boas, "A quantitative comparison of simultaneous bold fmri and nirs recordings during functional brain activation," *Neuroimage*, Vol. 17, pp. 719–731, 2002.

38. Toronov, V., A. Webb, J. H. Choi, M. Wolf, A. Michalos, E. Gratton, and D. Hueber, "Investigation of human brain hemodynamics by simultaneous near-infrared spectroscopy and functional magnetic resonance imaging," *Med. Phys.*, Vol. 28, pp. 521–527, 2001.

39. Fukui, Y., Y. Ajichi, and E. Okada, "Monte carlo prediction of near-infrared light propagation in realistic adult and neonatal head models," *Appl Opt.*, Vol. 42, no. 16, pp. 2881–2887, 2003.

40. Okada, E., and D. T. Delpy, "Near-infrared light propagation in an adult head model.ii. effect of superficial tissue thickness on the sensitivity of the near-infrared spectroscopy signal," *Appl Opt.*, Vol. 42, no. 16, pp. 2915–2922, 2003.

41. Cope, M., *The application of near-infrared spectroscopy to non-invasive monitoring of cerebral oxygenation in the newborn infant.* PhD thesis, University College London, London, United Kingdom, 1991.

42. Davis, T. L., K. K. Kwong, R. M. Weisskoff, and B. R. Rosen, "Calibrated functional mri: mapping dynamics of oxidative metabolism," *Proc Natl Acad Sci USA*, Vol. 95, no. 4, pp. 1834–1839, 1998.

43. Hoge, R. D., J. Atkinson, B. Gill, G. R. Crelier, S. Marrett, and G. B. Pike, "Investigation of the bold signal dependence on cerebral blood flow and oxygen consumption: the deoxyhemoglobin dilution model," *Magn Reson Med*, Vol. 42, no. 5, pp. 849–863, 1999.

44. Heekeren, H. R., H. Obrig, R. Wenzel, K. Eberle, J. Ruben, K. Villringer, R. Kurth, and A. Villringer, "Cerebral hemoglobin oxygenation during sustained visual stimulation-a near infrared spectroscopy study," *Philos Trans R Soc Lond B Biol Sci.*, Vol. 352, no. 1354, pp. 743–750, 1997.

45. Meek, J. H., C. E. Elwell, M. J. Khan, J. Romaya, J. S. Wyatt, D. T. Delpy, and S. Zeki, "Regional changes in cerebral hemodynamics as a result of a visual stimulus measured by near infrared spectroscopy," *Proc. Biol Sci.*, Vol. 261, no. 1362, pp. 351–356, 1995.

46. Sakatani, K., S. Chen, W. Lichty, H. Zuo, and Y. P. Wang, "Cerebral blood oxygenation changes induced by auditory stimulation in newborn infants measured by near infrared spectroscopy," *Early Hum. Dev.*, Vol. 55, no. 3, pp. 229–236, 1999.

47. Obrig, H., T. Wolf, C. Doge, J. J. Hulsing, U. Dirnagl, and A. Villringer, "Cerebral oxygenation changes during motor and somatosensory stimulation in humans, as measured by near-infrared spectroscopy," *Adv. Exp. Med. Biol.*, Vol. 388, pp. 219–224, 1996.

48. Colier, W. N., V. Quaresima, B. Oeseburg, and M. Ferrari, "Human motor-cortex oxygenation changes induced by cyclic coupled movements of hand and foot," *Exp. Brain Res.*, Vol. 129, no. 3, pp. 457–461, 1999.

49. Kleinschmidt, A., H. Obrig, M. Requardt, K. D. Merbolt, U. Dirnagl, A. Villringer, and J. Frahm, "Simultaneous recording of cerebral oxygenation changes during huma brain activation by magnetic resonance imaging and near-infrared spectroscopy," *J. Cereb Blood Flow Metab.*, Vol. 16, no. 5, pp. 817–826, 1996.

50. Sato, H., T. Takeuchi, and K. L. Sakai, "Temporal cortex activation during speech recognition: an optical topography study," *Cognition*, Vol. 73, no. 3, pp. B55–B66, 1999.

51. Sokol, D. K., O. N. Markand, E. C. Daly, T. G. Luerssen, and M. D. Malkoff, "Near infrared spectroscopy (nirs) distinguishes seizure types," *Cognition*, Vol. 9, no. 5, pp. 323–327, 2000.

52. Watanabe, E., A. Maki, F. Kawaguchi, Y. Yamashita, H. Koizumi, and Y. Mayagani, "Noninvasive cerebral blood volume measurement during seizures using multichannel near infrared spectroscopy topography," *J. Biomed. Opt.*, Vol. 5, no. 3, pp. 287–290, 2000.

53. Matsuo, K., T. Kato, M. Fukuda, and N. Kato, "Alteration of hemoglobin oxygenation in the frontal cortex region in elderly depressed patients as measured by near-infrared spectroscopy," *J. Neuropsychiatry Clin Neurosci.*, Vol. 12, no. 4, pp. 465–471, 2000.

54. Falgatter, A. J., M. Roesler, L. Sitzmann, A. Heidrich, T. J. Mueller, and W. K. Strik, "Loss of functional hemispheric asymmetry in alzheimer's dementia assessed with near infrared spectroscopy," *Brain Res Cogn. Brain Res.*, Vol. 6, no. 1, pp. 67–72, 1997.

55. Falgatter, A. J., and W. K. Strik, "Reduced frontal functional asymmetry in schizophrenia during a cued continuous performance test assessed with near-infrared spectroscopy," *Schizophr Bull*, Vol. 26, no. 4, pp. 913–919, 2000.

56. Okada, F., Y. Tokumitsu, Y. Hoshi, and M. Tamura, "Impaired interhemispheric integration in brain oxygenation and hemodynamics in schizophrenia," *Eur. Arch. Psychiatry Clin Neurosci.*, Vol. 244, no. 1, pp. 17–25, 1994.

57. Saitou, H., H. Yanagi, S. Hara, S. Tsuchiya, and S. Tomura, "Cerebral blood volume oxygenation among poststroke hemiplegic patients: effects of 13 rehabilitation tasks measured by near-infrared spectroscopy," *Arch. Phys. Med. Rehabil.*, Vol. 81, no. 10, pp. 1348–1356, 2000.

58. Vernieri, F., N. Rosato, F. Pauri, F. Tibuzzi, F. Passarelli, and P. M. Rossini, "Near infrared spectroscopy and transcranial doppler in monohemispheric stroke," *Eur. Neurol*, Vol. 41, no. 3, p. 159, 1999.

59. Emir, U. A., *Multimodal Investigation of fMRI and fNIRS derived Breath Hold BOLD Signals with an Expanded Balloon Model.* PhD thesis, Bogazici University, Istanbul, Turkey, 2008.

60. Huppert, T. J., *Hemodynamic-Based Inference of Cerebral Oxygen Metabolism.* PhD thesis, Harvard University, Massachusetts, USA, 2007.

61. Cope, M., D. T. Delpy, E. O. Reynolds, S. Wray, J. Wyatt, and P. van der Zee, "Methods of quantitating cerebral near infrared spectroscopy data," *Adv. Exp Med Biol.*, Vol. 222, pp. 183–189, 1988.

62. Kocsis, L., P. Herman, and A. Eke, "The modified beer-lambert law revisited," *Phys. Med. Biol.*, Vol. 51, no. 5, pp. N91–N98, 2006.

63. Strangman, G., M. A. Franceschini, and D. A. Boas, "Factors affecting the accuracy of near-infrared spectroscopy concentration calculations for the focal changes in oxygenation parameters," *Neuroimage*, Vol. 18, no. 4, pp. 865–879, 2003.

64. Sassaroli, A., and S. Fantini, "Comment on the modified beer-lambert law for scattering media," *Phys. Med. Biol.*, Vol. 49, no. 14, pp. N255–N257, 2004.

65. Arridge, S. R., "Optical tomography in medical imaging," *Inverse Probl*, Vol. 15, pp. R41–R93, 1999.

66. McCormick, P. W., M. Stewart, M. G. Goetting, M. Dujovny, G. Lewis, and J. I. Ausman, "Noninvasive cerebral optical spectroscopy for monitoring cerebral oxygen delivery and hemodynamics," *Crit. Care Med.*, Vol. 19, pp. 89–97, 1991.

67. McCormick, P. W., M. Stewart, G. Lewis, M. Dujovny, and J. I. Ausman, "Intracerebral penetration of infrared light," *J Neurosurg*, Vol. 76, pp. 315–318, 1992.

68. Kirilina, E., A. Jelzow, A. Heine, M. Niessing, H. Waibnitz, R. Bruhl, B. Itterman, A. M. Jacobs, and I. Tachtsidis, "The physiological origin of task-evoked systemic artefacts in functional near infrared spectroscopy," *Neuroimage*, Vol. 61, no. 1, pp. 70–81, 2012.

69. Al-Rawi, P. G., P. Smielewski, and P. J. Kirkpatrick, "Intracerebral penetration of infrared light," *Stroke*, Vol. 32, p. 2492Ğ2500, 2001.

70. Minati, L., I. U. Kress, E. Visani, N. Medford, and H. D. Critchley, "Intra- and extracranial effects of transient blood pressure changes on brain near-infrared spectroscopy (nirs) measurements," *J. Neurosci. Methods*, Vol. 197, pp. 283–288, 2011.

71. Tachtsidis, I., T. S. Leung, A. Chopra, P. H. Koh, C. B. Reid, and C. E. Elwell, *False positives in functional near infrared topography*, pp. 307–314. Oxygen Transport to Tissue, Boston, MA: Springer, 2009.

72. Takahashi, T., Y. Takikawa, R. Kawagoe, S. Shibuya, T. Iwano, and S. Kitazawa, "Influence of skin blood flow on near-infrared spectroscopy signals measured on the forehead during a verbal fluency task," *Neuroimage*, Vol. 57, pp. 91–1002, 2011.

73. Saager, R. B., N. L. Telleri, and A. J. Berger, "Two-detector corrected near infrared spectroscopy (c-nirs) detects hemodynamic activation responses more robustly than single-detector nirs," *Neuroimage*, Vol. 55, pp. 1679–1685, 2011.

74. Gregg, N. M., B. R. White, B. W. Zeff, A. J. Berger, and J. P. Culver, "Brain specificity of diffuse optical imaging: improvements from superficial signal regression and tomography," *Front. Neuroenergetics*, Vol. 2, no. 14, pp. 1–8, 2010.

75. Aletti, F., R. Re, V. Pace, D. Contini, E. Molteni, S. Cerutti, A. M. Bianchi, A. Torricelli, L. Spinelli, R. Cubeddu, and G. Baselli, "Deep and surface hemodynamic signal from functional time resolved transcranial near infrared spectroscopy compared to skin flowmotion," *Comput. Biol. Med.*, Vol. 42, no. 3, pp. 282–289, 2012.

76. Gagnon, L., R. J. Cooper, M. A. Yucel, K. L. Perdue, D. N. Greve, and D. A. Boas, "Short separation channel location impacts the performance of short channel regression in nirs," *Neuroimage*, Vol. 59, p. 2518Ğ2528, 2 2012.

77. Zhang, Q., G. Strangman, and G. Ganis, "Adaptive filtering to reduce global interference in non-invasive nirs measures of brain activation: How well and when does it work?," *Neuroimage*, Vol. 45, no. 3, pp. 788–794, 2009.

78. Tachtsidis, I., P. H. Koh, P. H. Stubbs, and C. E. Elwell, *Functional optical topography analysis using statistical parametric mapping (SPM) methodology with and without physiological confounds*, pp. 237–243. Oxygen Transport to Tissue, Boston, MA: Springer,, 2010.

79. Patel, S., T. Katura, A. Maki, and I. Tachtsidis, *Quantification of systemic interference in optical topography data during frontal lobe and motor cortex activation: an independent component analysis*, pp. 45–51. Oxygen Transport to Tissue, Boston, MA: Springer,, 2011.

80. Bandettini, P. A., E. C. Wong, R. S. Hinks, R. S. Tikofsky, and J. S. Hyde, "Time course epi of human brain function during task activation," *Magn. Reson. Med.*, Vol. 25, pp. 390–397, 1992.

81. Kwong, K. K., J. W. Belliveau, D. A. Chesler, I. E. Goldberg, R. M. Weisskoff, B. B. P. Poncelet, D. N. Kennedy, B. E. Hoppel, M. S. Cohen, and R. Turner, "Dynamic magnetic resonance imaging of human brain activity during primary sensory stimulation," *Proc. Natl. Acad. Sci. USA*, Vol. 89, pp. 5675–5679, 1992.

82. Ogawa, S., T. M. Lee, A. R. Kay, and D. W. Tank, "Brain magnetic resonance imaging with contrast dependent on blood oxygenation," *Proc. Natl. Acad. Sci. USA*, Vol. 87, p. 9868Ğ9872, 1990.

83. Ogawa, S., D. W. Tank, R. Menon, J. M. Ellerman, S. G. Kim, H. Merkle, and K. Ugurbil, "Intrinsic signal changes accompanying sensory stimulation: functional brain mapping with magnetic resonance imaging," *Proc. Natl. Acad. Sci. USA*, Vol. 89, p. 5951Ğ5955, 1992.

84. Buxton, R., *Introduction to Functional Magnetic Resonance Imaging: Principles and Techniques*, Cambridge University Press, 2002.

85. Coyle, S., *Near-infrared spectroscopy for brain computer interfacing.* PhD thesis, National University Of Ireland, Istanbul, Ireland, 2005.

86. van Zijl, P. C., S. M. Eleff, J. A. Ulatowski, J. M. Oja, A. M. Ulug, R. J. Traystman, and R. A. Kauppinen, "Dynamic magnetic resonance imaging of human brain activity during primary sensory stimulation," *Nat. Med.*, Vol. 4, pp. 159–167, 1998.

87. Thulborn, K. R., J. C. Waterton, P. M. Matthews, and G. K. Radda, "Oxygenation dependence of the transverse relaxation time of water protons in whole blood at high field," *Biochem. Biophy. Acta.*, Vol. 714, pp. 265–270, 1982.

88. Chu, S. C. K., Y. Xu, J. A. Balschi, and C. S. Springer, "Bulk magnetic susceptibility shifts in nmr studies of compartmentalized samples: Use of paramagnetic reagents," *Magn. Reson. Med.*, Vol. 13, pp. 239–262, 1990.

89. Hoppel, B. E., R. M. Weisskoff, K. R. Thulborn, J. B. Moore, K. K. Kwong, and B. R. Rosen, "Measurement of regional blood oxygenation and cerebral hemodynamics," *Magn. Reson. Med.*, Vol. 30, pp. 2715–723, 1993.

90. Bandettini, P. A., *Magnetic resonance imaging of human brain activation using endogenous susceptibility contrast.* PhD thesis, Faculty of the Graduate School of the Medical College of Wisconsin, Wisconsin, USA, 1994.

91. Uludag, K., D. J. Dubowitz, and R. B. Buxton, *Basic principles of functional MRI*, pp. 249–287. Philadelphia, PA: Saunders Elsevier, 3rd ed. ed., 2006.

92. Arridge, S. R., M. Cope, and D. T. Delpy, "The theoretical basis for the determination of optical pathlengths in tissue: temporal and frequency analysis," *Phys. Med. Biol.*, Vol. 37, pp. 1531–1560, 1992.

93. Cope, M., and D. T. Delpy, "System for long-term measurement of cerebral blood flow and tissue oxygenation on newborn infants by infrared transillumination," *Med. Biol. Eng.*, Vol. 37, pp. 1531–1560, 1988.

94. Delpy, D. T., M. Cope, P. van der Zee, S. Arridge, S. Wray, and J. Wyatt, "Estimation of optical pathlength through tissue from direct time of flight measurement," *Phys. Med. Biol*, Vol. 33, pp. 1433–1442, 1992.

95. Liebert, A., H. Waibnitz, J. Steinbrink, H. Obrig, M. Moller, R. MacDonald, A. Villringer, and H. Rinneberg, "Time-resolved multidistance near-infrared spectroscopy of the adult head: intracerebral and extracerebral absorption changes from moments of distribution of times of flight of photons," *Appl. Opt.*, Vol. 43, no. 3, pp. 3037–3047, 2004.

96. Wang, L.-H., S. L. Jacques, and L. Zheng, "Mcml- monte carlo modeling of light transport in multi-layered tissues," *Comput. Methods Programs Biomed.*, Vol. 47, pp. 131–146, 1995.

97. Wang, L.-H., and S. L. Jacques, *Optical Thermal Response of Laser Irradiated Tissue*, pp. 73–100. New York: Plenum Press, 1995.

98. Huppert, T. J., R. D. Hoge, M. A. Franceschini, and D. A. Boas, "A spatial-temporal comparison of fmri and nirs hemodynamic responses to motor stimuli in adult humans," *Proc. SPIE*, Vol. 5693, pp. 191–202, 2005.

99. Fang, Q., and D. A. Boas, "Monte carlo simulation of photon migration in 3d turbid media accelerated by graphics processing units," *Opt. Express*, Vol. 17, pp. 20178–20190, 2009.

100. Friston, K. J., J. Ashburner, S. J. Kiebel, T. E. Nichols, and W. Penny, *Statistical Parametric Mapping: the Analysis of Functional Brain Images*, London: Elsevier Academic Press, 2007.

101. Saager, R. B., and A. J. Berger, "Measurement of layer-like hemodynamic trends in scalp and cortex: implications for physiological baseline suppression in functional near-infrared spectroscopy," *J. Biomed. Opt*, Vol. 13, no. 3, pp. 034017–034017–10, 2008.

102. Devore, J. L., *Probability and Statistics for Engineering and the Sciences*, Vol. 4th ed., pp. 474–522. Belmont, California: Wadsworth Inc., 1995.

103. Sweeney, K., H. Ayaz, T. Ward, M. Izzetoglu, S. McLoone, and B. Onaral, "A methodology for validating artifact removal techniques for physiological signals," *IEEE Trans. Inf. Technol. Biomed.*, Vol. 16, no. 5, pp. 918–926, 2012.

104. Scholkmann, F., U. Gerber, M. Wolf, and U. Wolf, "End-tidal co2: An important parameter for a correct interpretation in functional brain studies using speech tasks," *Neuroimage*, Vol. 66, pp. 71–79, 2013.

105. Zeff, B. W., B. R. White, H. Dehghani, B. L. Schlaggar, and J. P. Culver, "Retinotopic mapping of adult human visual cortex with high-density diffuse optical tomography," *Proc. Natl. Acad. Sci. U.S.A*, Vol. 104, no. 29, pp. 12169–12174, 2007.

106. Fox, M. D., and M. E. Raichle, "Spontaneous fluctuations in brain activity observed with functional magnetic resonance imaging," *Nat. Rev. Neurosci.*, Vol. 8, pp. 700–711, 2007.

107. Cooper, R. J., L. Gagnon, D. Goldenholz, D. A. Boas, and D. N. Greve, "The utility of near- infrared spectroscopy in the regression of low-frequency physiological noise from functional magnetic resonance imaging data," *Neuroimage*, Vol. 59, pp. 3128–3138, 2011.

108. Frederick, B., L. M. Hocke, and Y. Tong, "Physiological denoising of bold fmri data using regressor interpolation at progressive time delays (riptide) processing of concurrent fmri and near-infrared spectroscopy (nirs)," *Neuroimage*, Vol. 60, pp. 1913–1923, 2012.

109. Zenker, W., and S. Kubik, "Brain cooling in humans-anatomical considerations," *Anat. Embryol.*, Vol. 193, no. 1, pp. 1–13, 1996.

110. Mesquita, R. C., M. A. Franceschini, and D. A. Boas, "Resting state functional connectivity of the whole head with near-infrared spectroscopy," *Biomed. Opt. Express*, Vol. 1, pp. 324–336, 2010.

111. Liebert, A., H. Waibnitz, J. Steinbrink, H. Obrig, M. Moller, R. MacDonald, A. Villringer, and H. Rinneberg, "Time-resolved multidistance near-infrared spectroscopy of the adult head: intracerebral and extracerebral absorption changes from moments of distribution of times of flight of photons," *Appl. Opt.*, Vol. 43, no. 3, pp. 3037–3047, 2004.

112. Wise, R. G., K. Ide, M. J. Poulin, and I. Tracey, "Resting fluctuations in arterial carbon dioxide induce significant low frequency variations in bold signal," *Neuroimage*, Vol. 21, no. 4, pp. 1652–1664, 2004.

113. Toronov, V., S. Walker, R. Gupta, J. H. Choi, E. Gratton, D. Hueber, and A. Webb, "The roles of changes in deoxyhemoglobin concentration and regional cerebral blood volume in the fmri bold signal," *Neuroimage*, Vol. 19, pp. 1521–1531, 2003.

114. Boxerman, J. L., P. A. Bandettini, K. K. Kwong, J. R. Baker, T. L. Davis, B. R. Rosen, and R. M. Weisskoff, "The intravascular contribution to fmri signal change: Monte carlo modeling and diffusion-weighted studies in vivo," *Magn. Reson. Med.*, Vol. 34, pp. 4–10, 1995.

115. Buxton, R. B., E. C. Wong, and L. R. Frank, "Dynamics of blood flow and oxygenation changes during brain activation: the balloon model," *Magn. Reson. Med*, Vol. 39, pp. 855–864, 1998.

116. Ogawa, S., R. S. Menon, D. W. Tank, S. G. Kim, H. Merkle, J. M. Ellerman, and K. Ugurbil, "Functional brain mapping by blood oxygenation level-dependent contrast magnetic resonance imaging. a comparison of signal characteristics with a biophysical model," *Biophys. J.*, Vol. 64, pp. 803–812, 1998.

117. Uludag, K., B. Muller-Bieri, and K. Ugurbill, "An integrative model for neuronal activity-induced signal changes for gradient and spin echo functional imaging," *Neuroimage*, Vol. 48, pp. 150–165, 2009.

118. Hoshi, Y., N. Kobayashi, and M. Tamura, "Interpretation of near-infrared spectroscopy signals: a study with a newly developed perfused rat brain model," *J. Appl. Physiol.*, Vol. 90, pp. 1657–1662, 2001.

119. MacIntosh, B. J., L. M. Klassen, and R. S. Menon, "Transient hemodynamics during a breath hold challenge in a two part functional imaging study with simultaneous near-infrared spectroscopy in adult humans.," *Neuroimage*, Vol. 20, pp. 1246–1252, 2003.

120. Siegel, A. M., J. P. Culver, J. B. Mandeville, and D. A. Boas, "Temporal comparison of functional brain imaging with diffuse optical tomography and fmri during rat forepaw stimulation.," *Phys. Med. Biol.*, Vol. 48, pp. 1391–1403, 2003.

121. Cui, X., S. Bray, D. M. Bryant, G. H. Glover, and A. L. Reiss, "A quantitative comparison of nirs and fmri across multiple cognitive tasks.," *Neuroimage*, Vol. 54, pp. 2808–2821, 2011.

122. Toronov, V. Y., X. Zhang, and A. G. Webb, "A spatial and temporal comparison of hemodynamic signals measured using optical and functional magnetic resonance imaging during activation in the human primary visual cortex.," *Neuroimage*, Vol. 34, pp. 1136–1148, 2007.

123. Drummond, P. D., "The effect of adrenergic blockade on blushing and facial blushing.," *Psychophysiology*, Vol. 34, pp. 163–168, 1997.

124. Hoshi, Y., and M. Tamura, "Detection of dynamic changes in cerebral oxygenation coupled to neuronal function during mental work in man.," *Neuroscience Letters*, Vol. 150, no. 1, pp. 5–8, 1993.

125. Tanida, M., K. Sakatani, r. Takano, and K. Tagai, "Relation between asymmetry of prefrontal cortex activities and the autonomic nervous system during a mental arithmetic task: near infrared spectroscopy study.," *Neuroscience Letters*, Vol. 369, pp. 69–74, 2004.

126. Tachtsidis, I., C. E. Elwell, T. S. Leung, C. W. Lee, M. Smith, and D. T. Delpy, "Investigation of cerebral haemodynamics by near-infrared spectroscopy in young healthy volunteers reveals posture-dependent spontaneous oscillations," *Physiol. Meas.*, Vol. 25, no. 14, pp. 437–445, 2004.

127. Heinzel, S., F. B. Haeussinger, T. Hahn, A. C. Ehlis, and A. J. Falgatter, "Variability of (functional) hemodynamics as measured with simultaneous fnirs and fmri during intertemporal choice.," *Neuroimage*, Vol. 369, no. 71C, pp. 125–134, 2013.

128. Tong, Y., and B. D. Frederick, "Time lag dependent multimodal processing of concurrent fmri and near-infrared spectroscopy (nirs) data suggests a global circulatory origin for low-frequency oscillation signals in human brain.," *Neuroimage*, Vol. 53, pp. 553–564, 2010.

129. Seiyema, A., J. Seki, H. C. Tanabe, I. Sase, A. Takatsuki, S. Miyauchi, H. Eda, S. Hayashi, T. Imaruoka, T. Iwakura, and T. Yanagida, "Circulatory basis of fmri signals: relationship between changes in the hemodynamic parameters and bold signal intensity," *Neuroimage*, Vol. 21, pp. 1204–1214, 2004.

130. Fabbri, F., A. Sassaroli, M. Henry, and S. Fantini, "Optical measurements of absorption changes in two-layered diffusive media," *Phys. Med. Biol.*, Vol. 49, p. 1183Ğ1201, 2004.